Composite Structures 359 (2025) 118945

Contents lists available at ScienceDirect

Composite Structures

journal homepage: www.elsevier.com/locate/compstruct

Optimization of critical buckling load for variable stiffness composites using the lamination parameters as the field variables

Eralp Demir [a,1,*], Ali Rashed [b,c]

[a] Department of Engineering Science, University of Oxford, Parks road, Oxford OX1 3PJ, UK
[b] Faculty of Engineering and Natural Sciences, Sabanci University, Istanbul, Turkey
[c] Integrated Manufacturing Technology Research and Application Center, Sabanci University, Istanbul, Turkey

ARTICLE INFO

Dataset link: https://github.com/EralpDemir/Composite-Materials

Keywords:
Variable stiffness
Buckling optimization
Tow steering
Lamination parameter
UMAT

ABSTRACT

Buckling is a critical design concern for thin-walled structures and fiber-reinforced composite materials because it occurs with much lower strains than in failure. In this study, an in-house code is developed to optimize the critical buckling load using the lamination parameters as a design variable. The manufacturing steering curvature constraints are directly applied on the lamination parameters for the first time during optimization. The variable stiffness design revealed an approximately 160% improvement in the buckling load with respect to the optimal constant stiffness. The improvement in the critical buckling load ratio is over 400% with respect to the quasi-isotropic case, which is consistent with previous findings (Wu et al., 2015). The critical buckling load is 27% less when two opposite edges are clamped and two opposite edges are free compared to the ideal simply supported out-of-plane displacement boundary conditions that were used in previous optimization studies (Wu et al., 2015, Hao et al. 2019, Wu et al. 2012, Setoodeh et al. 2009, IJsselmuiden et al. 2010). The critical load ratio serves as the objective function when Neumann boundary conditions are employed, since membrane reactions remain unchanged throughout the optimization process, unlike in the case of Dirichlet boundary conditions. In addition, a widely accepted optimum fiber angle distribution, suggested in Gürdal et al. (2008), is implemented in a user-defined subroutine (UMAT) of Abaqus® to compare the buckling response of constant and variable stiffness of a plate.

1. Introduction

Current state-of-the-art developments in manufacturing automation together with digitization have been driving towards automated composite manufacturing processes. For this reason, the automated fiber placement method (AFP) has been used to support hand layup techniques in composite manufacturing to minimize defects induced by human interaction [1]. The AFP method has been performed with the a robotic manipulator laying multiple tows which is especially useful for manufacturing components with curved surfaces. AFP offers an additional functionality that enables the steering of tows within the plane of a layer with limitation on the steering curvature.

AFP method offers flexibility in the design of composite structures with variable stiffness (VS) by steering the tows in the plane of a layer of a composite structure for better mechanical performance [2]. VS composites in an AFP context usually refer to in-plane variation of stiffness by steering of tows instead of stiffness variation due to thickness changes or ply drop-offs. The radius of the steering curvature is considered to be the major manufacturing limitation, and hence a design constraint. Generally, the unit composite structure consists of cylindrical shells [3,4] or plates and panels [5,6] that have been studied to understand the fundamental principles for the design and manufacture of the AFP process. However, the curvature limit pushes towards large sample sizes, making experimental investigations challenging [7].

Design optimization methods have been used to maximize the mechanical performance of composite materials [8,9]. Optimization methods used different objective functions such as mass [10,11], strength or failure [12–15], stiffness or compliance [16–18], vibrational characteristics (natural frequency) [19–21], and buckling load [22–28]. Among these design methods, the design for buckling has been found to be critical because it occurs before the failure of thin-walled composite structures. Various design variables include fiber angles, stacking sequence, thickness, polar variable, or lamination parameters.

The lamination parameters are highly effective at transforming optimization into a convex problem, making a global optimal solution

* Corresponding author.
E-mail address: eralp.demir@eng.ox.ac.uk (E. Demir).
[1] Post-Doctoral Researcher.

https://doi.org/10.1016/j.compstruct.2025.118945
Received 12 September 2024; Received in revised form 25 December 2024; Accepted 5 February 2025
Available online 13 February 2025
0263-8223/© 2025 The Authors. Published by Elsevier Ltd. This is an open access article under the CC BY license (http://creativecommons.org/licenses/by/4.0/).

possible through the use of efficient gradient-based optimizers. The objective function becomes a linear function of the lamination parameters [29]. The lamination parameters convert the optimization to a convex domain that allows a global optimum [19]. Therefore, a feasible nonlinear region must be identified for the inequality constraints in the lamination parameter space [30]. Recently, Wu et al. [31] derived inequality constraints for a feasible convex domain for optimization for specially orthotropic materials, which is a function of both in-plane and out-of-plane stiffness. In their work, the proposed convex feasible domain agrees with the earlier findings of Grenestedt and Gudmundson [32].

Optimal lamination parameters need to be converted into fiber angles and stacking sequences. In some studies, this is achieved by genetic algorithms [33] that were used as a second-level optimization step after optimization of the lamination parameter for the best performance. For laminates with fewer than ten layers, direct search methods were found to reveal effective results [34]. However, the local selection of the fiber angles does not ensure fiber continuity. Therefore, an additional measure on the curvature constraint was introduced to ensure the manufacturability of the VS layup design [35].

The design of a manufacturable composite material for tow steering has been a great challenge because angles shall be considered as a design variable. The main design variable in this case is the local curvature for the tow steering process [36]. For this reason, optimization methods have been used to include local curvature as a design constraint [37]. Similarly, polar design variables were used to find the fiber directions with steering limitations [38]. In addition, constraints on the distribution of lamination parameters were also applied to ensure a uniform distribution of fiber angles indirectly but effectively, previously using cellular automata [39], finite element interpolation functions [17], and more recently using B-splines [31,40]. Consequently, a finite element-based method was developed that enforces fiber continuity within a given curvature limit (LSC method) to determine fiber angles for various design cases [34,41,42]. Furthermore, streamline functions were used to convert fiber angle distributions to manufacturable paths [43,44]. Tow parallelism was used as an additional constraint in the optimization algorithm to ensure the continuity of tows [45]. Therefore, it is essential to apply manufacturing constraints during the design stage.

This research presents a design optimization approach utilizing lamination parameters to enhance the buckling load of composite structures by directly imposing manufacturing constraints on the design variables within a single-tier gradient-based optimization process. The lamination parameters are defined as field variables, with their continuity upheld by penalizing non-zero gradients during optimization. This approach is novel in ensuring the curvature constraint necessary for manufacturability. The process of transforming lamination parameters into a layup sequence, which consists of fiber angles and layer thicknesses, involves a direct search method. This is subsequently followed by the conversion of the tow-angle distributions into precise paths, utilizing streamlines as input for the manufacturing machine. The approach is utilized to analyze compression buckling in a plate. A comparison is made between the variable stiffness optimization results for a practical clamped–clamped–free–free boundary condition and the ideal simply supported out-of-plane boundary condition, which is frequently cited in many Refs. [31,46]. The results produced by the in-house code are consistent with both experimental and numerical findings reported in the literature. Furthermore, the optimal compression buckling design presented by [46] is evaluated using Abaqus® alongside its UMAT subroutine to specify material characteristics. The results are then compared with scenarios that involve constant stiffness to demonstrate the efficacy of their design optimization approach.

The outline of the paper is as follows. Section 2 introduces the method used for buckling optimization, Section 3 includes a validation of the proposed approach with comparison with the numerical and experimental findings in the literature. Sections 4 and 5 contain the results and conclusions, respectively.

2. Model description

This section describes the overall methodology used to optimize the buckling response of a plate. The following subsections include a detailed explanation on the finite element framework in Section 2.1, lamination parameter continuity constraint in Section 2.2, gradient-based buckling optimization method in Section 2.3, conversion of the optimum lamination parameters to the fiber angles in Section 2.4, steering curvature in Section 2.5, path generation in Section 2.6, and the overall numerical implementation in Section 2.7.

2.1. Finite element method

The critical buckling load ratio, λ_1, is determined through the generalized eigenvalue problem in which $[\mathbf{K}_b]$, $[\mathbf{K}_G]$, $\{\mathbf{a}_i\}$, λ_i represent the global bending stiffness matrix, the global geometric stiffness matrix, the eigenvectors, and the eigenvalues of the system, respectively:

$$([\mathbf{K}_b] - \lambda_i [\mathbf{K}_G])\{\mathbf{a}_i\} = \mathbf{0} \quad i = 1, 2, \ldots, n. \tag{1}$$

The sensitivity of ith eigenvalue, λ_i, with respect to the lamination parameters as the design variable, $\{\xi\}$, is computed by differentiation of Eq. (1) giving:

$$\frac{\partial \lambda_i}{\partial \{\xi\}} = \left(\{\mathbf{a}_i\}^T \frac{\partial [\mathbf{K}_b]}{\partial \{\xi\}} \{\mathbf{a}_i\} - \lambda_i \{\mathbf{a}_i\}^T \frac{\partial [\mathbf{K}_G]}{\partial \{\xi\}} \{\mathbf{a}_i\} \right) / \{\mathbf{a}_i\}^T [\mathbf{K}_G] \{\mathbf{a}_i\}. \tag{2}$$

The design variable for each finite element, $\{\xi\}$, contains both in-plane and out-of-plane lamination parameters, in vectorized form:

$$\{\xi\} = \left\{ \xi_1^A \quad \xi_3^A \quad \xi_1^D \quad \xi_3^D \right\}^T. \tag{3}$$

The bending stiffness depends exclusively on the bending lamination parameters, ξ_1^D and ξ_3^D, similar to how the stiffness in the plane is solely determined by the membrane lamination parameters. The bending stiffness matrix of a finite element $[\mathbf{k}_b]$ is computed using the strain–displacement mapping, $[\mathbf{B}]$, and bending material stiffness matrix, $[\mathbf{D}]$:

$$[\mathbf{k}_b] = \int_S [\mathbf{B}]^T [\mathbf{D}] [\mathbf{B}] \, \mathrm{d}S. \tag{4}$$

Orthotropic material stiffness is a linear function of the out-of-plane (or bending) lamination parameters, ξ_1^D and ξ_3^D:

$$\{\mathbf{D}\} = \frac{t^3}{12} [\mathbf{U}] \left\{ 1 \quad \xi_1^D \quad 0 \quad \xi_3^D \quad 0 \right\}^T. \tag{5}$$

The material invariant, $[\mathbf{U}]$, is independent of the fiber angle or thickness which is defined as:

$$[\mathbf{U}] = \begin{bmatrix} U_1 & U_2 & 0 & U_3 & 0 \\ U_4 & 0 & 0 & -U_3 & 0 \\ U_1 & -U_2 & 0 & U_3 & 0 \\ 0 & 0 & U_2/2 & 0 & U_3 \\ 0 & 0 & U_2/2 & 0 & -U_3 \\ (U_1 - U_4)/2 & 0 & 0 & -U_3 & 0 \end{bmatrix}. \tag{6}$$

The material stiffness matrix can be expressed in terms of the lamina stiffness constants of Q_{11}, Q_{22}, Q_{12} and Q_{66} as:

$$\begin{aligned} U_1 &= (3Q_{11} + 3Q_{22} + 2Q_{12} + 4Q_{66})/8, \\ U_2 &= (Q_{11} - Q_{22})/2, \\ U_3 &= (Q_{11} + Q_{22} - 2Q_{12} - 4Q_{66})/8, \\ U_4 &= (Q_{11} + Q_{22} + 6Q_{12} - 4Q_{66})/8. \end{aligned} \tag{7}$$

The lamina stiffness constants are calculated from lamina elastic moduli; E_{11}, E_{22}, Poisson's ratio ν_{12}, and shear modulus G_{12}:

$$\begin{aligned} Q_{11} &= E_{11}^2/(E_{11} - \nu_{12}^2 E_{22}), \\ Q_{12} &= \nu_{12} E_{11} E_{22}(E_{11} - \nu_{12}^2 E_{22}), \end{aligned} \tag{8}$$

$$Q_{22} = E_{11}E_{22}/(E_{11} - \nu_{12}^2 E_{22}),$$
$$Q_{66} = G_{12}.$$

The bending strain–displacement mapping which is used to compute the bending stiffness matrix, $[\mathbf{B}]$, is obtained by the partial spatial derivatives interpolation function vector. $\{\mathbf{N}\}$, represents the shape functions of Bogner–Fox–Schmit (BFS) type plate elements:

$$[\mathbf{B}] = \begin{bmatrix} \frac{\partial^2 \{\mathbf{N}\}}{\partial x^2} \\ \frac{\partial^2 \{\mathbf{N}\}}{\partial y^2} \\ \frac{\partial^2 \{\mathbf{N}\}}{\partial x\, \partial y} \end{bmatrix}. \tag{9}$$

The differentiation of elemental bending stiffness matrix in Eq. (4) with respect to the design variable (out-of-plane lamination parameters) gives the sensitivity of bending stiffness:

$$\frac{\partial \left[\mathbf{k}_b\right]}{\partial \{\boldsymbol{\xi}^D\}} = \int_S [\mathbf{B}]^T \frac{\partial [\mathbf{D}]}{\partial \{\boldsymbol{\xi}^D\}} [\mathbf{B}]\, \mathrm{d}S. \tag{10}$$

The partial derivative of vectorized bending stiffness, $\frac{\partial [\mathbf{D}]}{\partial \{\boldsymbol{\xi}^D\}}$, is obtained by considering the two of the indepedent components of the out-of-plane lamination parameters, ξ_1^D and ξ_3^D, separately as:

$$\frac{\partial \{\mathbf{D}\}}{\partial \xi_1^D} = \frac{t^3}{12} [\mathbf{U}] \{0\ 1\ 0\ 0\ 0\}^T, \tag{11}$$

$$\frac{\partial \{\mathbf{D}\}}{\partial \xi_3^D} = \frac{t^3}{12} [\mathbf{U}] \{0\ 0\ 0\ 1\ 0\}^T. \tag{12}$$

The geometric stiffness matrix or stress stiffening, $\left[\mathbf{K}_G\right]$, is computed in terms of the in-plane stress, $[\sigma]$, and the gradients, $[\mathbf{G}]$ as:

$$\left[\mathbf{K}_G\right] = \int_S [\mathbf{G}]^T [\sigma] [\mathbf{G}]\, \mathrm{d}S. \tag{13}$$

$[\mathbf{G}]$ is the gradient mapping that is computed using the Bogner–Fox–Schmit interpolation function vector, $\{\mathbf{N}\}$, in the plane along both x and y directions:

$$[\mathbf{G}] = \begin{bmatrix} \frac{\partial \{\mathbf{N}\}}{\partial x} \\ \frac{\partial \{\mathbf{N}\}}{\partial y} \end{bmatrix}. \tag{14}$$

Eq. (15) shows the components of the in-plane two-dimensional stress matrix:

$$\boldsymbol{\sigma} = \begin{bmatrix} \sigma_{xx} & \sigma_{xy} \\ \sigma_{xy} & \sigma_{yy} \end{bmatrix}. \tag{15}$$

In-plane (membrane) stresses for a finite element, $[\sigma]$, are calculated using the membrane stiffness matrix, $[\mathbf{A}]$, membrane strain–displacement mapping, $\left[\mathbf{B}_m\right]$, and membrane displacements, $\left\{\mathbf{d}_m\right\}$ using Eq. (16). Note that these all quantities are computed for each element individually:

$$[\sigma] = [\mathbf{A}] \left[\mathbf{B}_m\right] \left\{\mathbf{d}_m\right\}. \tag{16}$$

The membrane strain–displacement mapping is calculated from the partial derivatives of in-plane shape functions of a linear quadrilateral element with four nodes,[2] $N_m^{(j)}$:

$$\left[\mathbf{B}_m\right] = \begin{bmatrix} \frac{\partial N_m^{(1)}}{\partial x} & 0 & \cdots & \frac{\partial N_m^{(4)}}{\partial x} & 0 \\ 0 & \frac{\partial N_m^{(1)}}{\partial y} & \cdots & 0 & \frac{\partial N_m^{(4)}}{\partial y} \\ \frac{\partial N_m^{(1)}}{\partial y} & \frac{\partial N_m^{(1)}}{\partial x} & \cdots & \frac{\partial N_m^{(4)}}{\partial y} & \frac{\partial N_m^{(4)}}{\partial x} \end{bmatrix}. \tag{17}$$

[2] The superscript in parenthesis represent the node number of a finite element.

The orthotropic material in-plane stiffness, $\{\mathbf{A}\}$, is computed in terms of the two in-plane lamination parameters, ξ_1^A and ξ_3^A:

$$\{\mathbf{A}\} = t\, [\mathbf{U}] \left\{1 \quad \xi_1^A \quad 0 \quad \xi_3^A \quad 0\right\}^T. \tag{18}$$

The differentiation of geometric stiffness matrix in Eq. (2), with respect to the in-plane lamination parameters gives:

$$\frac{\partial \left[\mathbf{K}_G\right]}{\partial \{\boldsymbol{\xi}\}} = \int_S [\mathbf{G}]^T \left(\frac{\partial [\mathbf{A}]}{\partial \{\boldsymbol{\xi}^A\}} \left[\mathbf{B}_m\right] \left\{\mathbf{d}_m\right\} + [\mathbf{A}] \left[\mathbf{B}_m\right] \frac{\partial \left\{\mathbf{d}_m\right\}}{\partial \{\boldsymbol{\xi}^A\}} \right) [\mathbf{G}]\, \mathrm{d}S. \tag{19}$$

The partial derivatives of vectorized in-plane stiffness, $\{\mathbf{A}\}$, with respect to the components of the in-plane lamination parameter components, ξ_1^A and ξ_3^A are:

$$\frac{\partial \{\mathbf{A}\}}{\partial \xi_1^A} = t\, [\mathbf{U}] \{0\ 1\ 0\ 0\ 0\}^T, \tag{20}$$

$$\frac{\partial \{\mathbf{A}\}}{\partial \xi_3^A} = t\, [\mathbf{U}] \{0\ 0\ 0\ 1\ 0\}^T. \tag{21}$$

The global in-plane (membrane) equilibrium in terms of the external in-plane forces, $\left\{\mathbf{p}_m\right\}$, in-plane displacements, $\left\{\mathbf{d}_m\right\}$, and membrane stiffness, $\left[\mathbf{K}_m\right]$ gives:

$$\left[\mathbf{K}_m\right] \left\{\mathbf{d}_m\right\} = \left\{\mathbf{p}_m\right\}. \tag{22}$$

The differentiation of global in-plane equilibrium, allows calculation of the membrane displacement derivatives. The in-plane loads, $\left\{\mathbf{p}_m\right\}$, are assumed to be constant during optimization [22] when the Neumann boundary conditions were used. However, the membrane reactions will not remain constant during optimization when Diriclet boundary conditions were used. Many of the former studies [31,46,47] used displacement boundary conditions (uniform end shortening) instead of force boundary conditions neglecting the change in the reaction forces. Indeed this alters the reaction forces then the optimization problem is not the maximization of load ratio but it shall be maximization of the critical buckling load which is obtained by multiplying the membrane reaction forces with the critical load ratio. To be consistent with the optimization formulation [48], force boundary conditions shall be used instead of uniform displacements.

Eq. (23) contains the inverse of the global membrane stiffness, $\left[\mathbf{K}_m\right]^{-1}$. This is calculated by application of the in-plane boundary conditions to eliminate the singularity of the membrane stiffness before inversion to find membrane displacement derivatives with respect to the lamination parameters:

$$\frac{\partial \left\{\mathbf{d}_m\right\}}{\partial \{\boldsymbol{\xi}^A\}} = -\left[\mathbf{K}_m\right]^{-1} \frac{\partial \left[\mathbf{K}_m\right]}{\partial \{\boldsymbol{\xi}^A\}} \left\{\mathbf{d}_m\right\}. \tag{23}$$

The global membrane stiffness, $\left[\mathbf{K}_m\right]$, is obtained by regular finite element assembly of elemental membrane stiffness, $\left[\mathbf{k}_m\right]$, which is computed using:

$$\left[\mathbf{k}_m\right] = \int_S \left[\mathbf{B}_m\right]^T [\mathbf{A}] \left[\mathbf{B}_m\right] \mathrm{d}S. \tag{24}$$

Differentiation of elemental membrane stiffness with respect to the design variable reveals:

$$\frac{\partial \left[\mathbf{K}_m\right]}{\partial \{\boldsymbol{\xi}^A\}} = \int_S [\mathbf{B}_m]^T \frac{\partial [\mathbf{A}]}{\partial \{\boldsymbol{\xi}^A\}} \left[\mathbf{B}_m\right] \mathrm{d}S. \tag{25}$$

With Eqs. (1) and (2), the objective function for the optimization, and its derivatives can be obtained analytically.

2.2. Lamination parameter continuity constraint

The continuous fiber placement is essential to maintain the strength of composite materials. This demands continuous tow steering, which was previously achieved by enforcing the continuity of the fiber angles [37,41,42,49]. However, in this study, the lamination parameters

are used as the field variables instead of fiber angles, and their gradient (in-the-plane) along the x and y directions is set to zero, which is referred to as the continuity constraint.

The least squares fit and continuity are enforced simultaneously to find the distribution of the lamination parameters, $\boldsymbol{\xi}(\mathbf{x})$. The goal is to have the minimum difference from the optimum lamination parameters, $\boldsymbol{\xi}_{opt}$. Therefore, the local form of the residual becomes:

$$\boldsymbol{\xi}(\mathbf{x}) - \boldsymbol{\xi}_{opt} = \mathbf{0}. \tag{26}$$

The continuity is enforced by setting the gradient of each element of the lamination parameter vector to zero:

$$\boldsymbol{\nabla}\boldsymbol{\xi}(\mathbf{x}) = \mathbf{0}. \tag{27}$$

These two constraints are coupled to solve for the field variable. A penalty factor, α, is used for the continuity constraint:

$$\boldsymbol{\xi}(\mathbf{x}) + \alpha\, \boldsymbol{\nabla}\boldsymbol{\xi}(\mathbf{x}) \cdot \boldsymbol{\nabla}\boldsymbol{\xi}(\mathbf{x}) = \boldsymbol{\xi}_{opt}. \tag{28}$$

Multiplying the local constraints by weight functions and integrating, the weak form is obtained:

$$([\mathbf{L}] + \alpha\,[\mathbf{C}])\,\{\boldsymbol{\xi}\} = \{\mathbf{q}\}. \tag{29}$$

Least squares constraint, $[\mathbf{L}]$, is expressed in terms of the shape functions, $\{\mathbf{N}\}$, of a linear quadrilateral:

$$[\mathbf{L}] = \int_{\Omega} \{\mathbf{N}\}^T \{\mathbf{N}\}\, \mathrm{d}\Omega. \tag{30}$$

Continuity constraint, $[\mathbf{C}]$, penalizes the gradients along x and y directions which is calculated in terms of the derivatives of the weight functions, $\{\boldsymbol{\nabla}\mathbf{N}\}$:

$$[\mathbf{C}] = \int_{\Omega} \{\boldsymbol{\nabla}\mathbf{N}\}^T \{\boldsymbol{\nabla}\mathbf{N}\}\, \mathrm{d}\Omega. \tag{31}$$

Optimum lamination parameters are used construct a force-like vector:

$$\{\mathbf{q}\} = \int_{\Omega} \{\mathbf{N}\}^T \boldsymbol{\xi}_{opt}\, \mathrm{d}\Omega. \tag{32}$$

This penalization is applied during calculation of the objective function after the optimization retrieves lamination parameters during the optimization cycles.

2.3. Optimization

The objective function maximizes the first buckling load in terms of the minimizer, $\boldsymbol{\xi}(\boldsymbol{x})$:

$$\min\left[-\lambda_1\left(\boldsymbol{\xi}(\boldsymbol{x})\right)\right]. \tag{33}$$

Section 2.1 shows the objective function and its gradient with respect to the design variables. The objective functions for CS and VS cases are calculated in separate functions; "OPT_objective_con" and "OPT_objective_var". Appendix E shows the details on the code structure.

Buckling is a coupled problem in terms of in-plane and out-of-plane stiffness. Therefore, the feasible domain is different from problems that involve only in-plane or only out-of-plane stiffnesses such as compliance optimization [34] or natural frequency optimization [49].

The lamination parameter at any position as a field variable, $\boldsymbol{\xi}(\boldsymbol{x})$, is obtained using the lamination parameter at each node $\boldsymbol{\xi}_{node}$. The specially-orthotropic materials have four independent lamination parameters that are the same throughout the plate for constant stiffness (CS) case while they are defined as a separate variable for each node of the finite element mesh for the variable stiffness (VS) case:

$$\boldsymbol{\xi}_{node} = \left\{\xi_1^A \quad \xi_3^A \quad \xi_1^D \quad \xi_3^D\right\}_{node}^T. \tag{34}$$

The inequality constraint functions, g_i, are expressed in terms of the lamination parameters in accordance with the Ref. [31] as:

$$5\,(\xi_1^A - \xi_1^D)^2 - 2\,[1 + \xi_3^A - 2(\xi_1^A)^2] \le 0, \tag{35}$$

$$(\xi_3^A - 4r\xi_1^A + 1 + 2r^2)^3 - 4(1 + 2\,|r| + r^2)\,(\xi_3^D - 4r\xi_1^D + 1 + 2h^2) \le 0, \tag{36}$$

$$(4r\xi_1^A - \xi_3^A + 1 + 4\,|r|)^3 - 4(1 + 2\,|r| + r^2)^2\,(4r\xi_1^D - \xi_3^D + 1 + 4\,|r|) \le 0. \tag{37}$$

The parameter r takes the values that are shown in Eq. (38) which results in a total of 19 non-linear inequality constraints:

$$r = \begin{bmatrix} -1 & -0.75 & -0.5 & -0.25 & 0 & 0.25 & 0.5 & 0.75 & 1 \end{bmatrix}. \tag{38}$$

Linear inequality constraints in the optimization are defined as:

$$-1 \le \xi_1^A \le 1, \quad -1 \le \xi_3^A \le 1, \quad -1 \le \xi_1^D \le 1, \quad -1 \le \xi_3^D \le 1. \tag{39}$$

The optimization requires the gradient of the constraints in Eqs. (35)–(37) which is relatively simple to calculate. However, the optimizer also demands for the gradient of the objective function (tangent), which has an intricate calculation procedure explained in Section 2, and if not provided, the optimizer calculates the tangent using a method similar to perturbation that takes a significant amount of computational time. The gradient of the objective function is verified using the numerical perturbation as a second means to check, which is explained in detail in the Appendix B.

Optimization was performed using the Matlab® fmincon library. These optimization constraints for the CS and VS cases are defined in different functions in (OPT_constraint_con.m) and (OPT_constraint_var.m), respectively. The description of functions is provided within Appendix E The interior point algorithm is selected as the optimization method to ensure a solution in the feasible domain. The convergence tolerances for constraints tolerance, step tolerance and optimal tolerance, were set to 10^{-6} in this study to perform optimization in reasonable computational time.

2.4. Conversion of lamination parameters to fiber angles

The lamination parameters are converted into fiber angles using a direct search algorithm. A library consisting of conventional or non-conventional lamina angles is constructed and the corresponding lamination parameters are computed once at the beginning of the optimization. Angles are chosen for the specially orthotropic case in which a single angle defines all remaining angles for an eight-layer laminate [50]. Therefore, the angles of the specially orthotropic laminate with the least number of layers (eight layers [50]) have the form as $[-\theta/\theta/\theta/-\theta/\theta/-\theta/-\theta/\theta]$ or in abbreviated form as $[[-\theta/\theta/\mathrm{S}]/\mathrm{A}]$ which assures zero coupling between normal stresses and twisting curvature [50]. Optimal fiber angles, θ_{opt}, and stacking sequence, z, are determined by finding the possible laminate configuration that has the closest value to the optimum lamination parameters, $\boldsymbol{\xi}_{opt}$ using the direct search method among possible configurations, $\boldsymbol{\xi}(\theta_{opt}, z)$. This is performed for all of the elements in the finite-element mesh by using the vectorized form in Eq. (40).

$$\min\left(\left|\{\boldsymbol{\xi}(\theta_{opt}, z)\} - \{\boldsymbol{\xi}_{opt}\}\right|\right). \tag{40}$$

2.5. Steering curvature

The curvature for each finite element, κ_{el}, is calculated for plotting and visualization purposes. The elemental quantities $\{\boldsymbol{\theta}_{el}\}$, $[\mathbf{C}_{el}]$ and ω refer to the angle of the fiber at the nodes, the continuity constraint matrix, and the domain of the element, respectively:

$$\kappa_{el}^2 = \{\boldsymbol{\theta}_{el}\}^T [\mathbf{C}_{el}]\, \{\boldsymbol{\theta}_{el}\}\, /4\,\omega. \tag{41}$$

The penalty factor for the continuity constraint, α, is determined from the maximum allowable limit for elemental (or local) curvatures, κ_{el}^{max}. Optimization can be performed for a single penalty factor that is the same for the whole plate.

2.6. Path generation

The computer-aided system for composites manufacturing by the tow steering process demands guide curves in the form of splines as the main input for the tow paths. Therefore, the distribution of manufacturable fiber angles, $\theta(\mathbf{x})$, shall be converted into tow paths and entered into the software as input. The conversion of angles to paths was performed using the streamline analogy [51].

Eq. (42) defines a stream function, $\Psi(x, y)$, and for each value of C a streamline can be obtained.

$$\Psi(x, y) = C. \tag{42}$$

This problem was reduced to a linear problem by introducing natural logarithm of thickness function,[3] h, and given fiber angles, θ according to:

$$-\mathbf{s}\,\nabla \ln(h) = \mathbf{n}\,\nabla\theta. \tag{43}$$

In which $\mathbf{s}$ and $\mathbf{n}$ represent tangent and normal directions, respectively, that can be calculated in terms of the direction cosines of the velocity vector:

$$\mathbf{s} = \begin{Bmatrix} \cos\theta \\ \sin\theta \end{Bmatrix}. \tag{44}$$

$$\mathbf{n} = \begin{Bmatrix} -\sin\theta \\ \cos\theta \end{Bmatrix}. \tag{45}$$

The gradient of the fiber angles are obtained according to:

$$\boldsymbol{\nabla}\theta = \begin{Bmatrix} \theta_{,x} \\ \theta_{,y} \end{Bmatrix}. \tag{46}$$

The gradient of the natural logarithm of the thickness function, h, is related to the gradient of the thickness function as:

$$\nabla \ln(h) = \begin{Bmatrix} h_{,x}/h \\ h_{,y}/h \end{Bmatrix}. \tag{47}$$

The global form of Eq. (43) can be obtained by multiplying by a weight function and integrating to give Eq. (48). The same weight functions can be used to compute the gradients. In this relation $[\mathbf{D}]$, $\{\mathbf{e}\}$, and $\{\mathbf{f}\}$ represent the global constraint in matrix form, vector of the natural logarithm of the thickness function, and a vector consisting of given tow angle gradients, respectively.

$$[\mathbf{D}]\{\mathbf{e}\} = \{\mathbf{f}\}. \tag{48}$$

This study is to provide the tow paths in the form spline functions to be used as guide curves by the manufacturing system. Individual tow geometries will be determined by commercial software, such as CADFiber® that is compatible with the Coriolis® AFP system. The discretization of tows can be different depending on the tow width and dimensions depending on the number of tows that would be laid simultaneously during the manufacturing process. This justifies the use of a different discretization in both FEM and streamline analyses.

2.7. Numerical implementation

An open-source in-house code is implemented using MATLAB® that is available on Github [52]. The m-files with the prefixes "FEM", "MAT", "LP", "LSC", and "OPT" contain the functions related to the finite element analysis for buckling, material stiffness, lamination parameters, discretized least-squares constraints on lamination parameters, and optimization, respectively. The detailed description of the functions and their descriptions is given in the Appendix E.

Section 3 is dedicated to the experimental and numerical validation of the proposed in-house code. In addition, Appendix D includes the comparison of the in-house code with a commercial solver.

[3] Thickness function refers to a different property than the actual thickness of the plate.

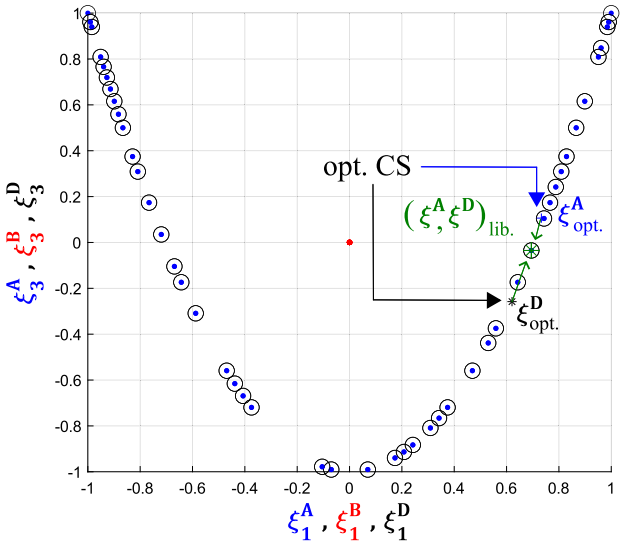


Fig. 1. Lamination parameters (ξ^A, ξ^B, ξ^D in blue, red, and black colors, respectively) for an eight-layered specially-orthotropic laminate with 1° fiber angle interval. The marked location indicates the coordinates for the optimum CS case and corresponding nearest specially-orthotropic laminate coordinates in the lamination parameter library (in green color).

In Section 4,specially orthotropic laminate configuration is used to transform the optimal lamination parameters into fiber angles and the stacking sequence. The layer thickness is assumed to remain constant considering the practical applications of the Automated Fiber Placement (AFP) process. Although the thickness of the towpreg material is ideally unchanged, it is in reality expected to fluctuate after the manufacturing process due to overlaps and gaps. Furthermore, it is assumed that the laminate design consists of a total of eight layers. This initial setup enables rapid computation of possible lay-up sequences early in the analysis, facilitating the creation of a material library containing potential layup configurations. In an eight-layer specially orthotropic laminate, the total number of candidate materials, N, is equivalent to the number of possible fiber orientations [50]. The optimal lamination parameters are translated into a layup sequence employing a direct search approach. This method finds the smallest distance within the lamination parameter space among the N candidate layups, as described in Eq. (40).

Fig. 1 shows the possible lamination parameters for the 1° fiber angle interval and the eight-layered specially-orthotropic laminate. The optimum values of the in-plane and out-of-plane lamination parameters were marked as blue dots and black circles, respectively. The optimum lamination parameters (green star symbol) in Fig. 1, are then converted to the specially orthotropic case in the library by finding the nearest point according to Eq. (40) as shown schematically. The material properties and plate dimensions are as in [31,47,53–55]. Table 1 shows the material parameters used in the simulations in Section 4. The size of the square plate (with a width and height of a and b, respectively, having equal dimensions) was 254 mm with an overall thickness of 1.016 mm. Two types of boundary conditions were used for out-of-plane displacements: simply supported edges (SSSS) and clamped–clamped–free–free edges (CCFF). In-plane boundary conditions were clamped–clamped–free–free (CCFF). The input loads were two types of uniform displacement of 1 mm or a uniformly distributed load of 1 N/mm on the top edge of the plate along the negative y-direction. The boundary conditions were similar to case-2 in [55] and case-A in [31]. A mesh with 15 elements per edge was used.

The use of displacement (Diriclet) boundary conditions as input leads to a change in membrane reaction forces during optimization. Thus, the objective function shall be modified to maximize the critical

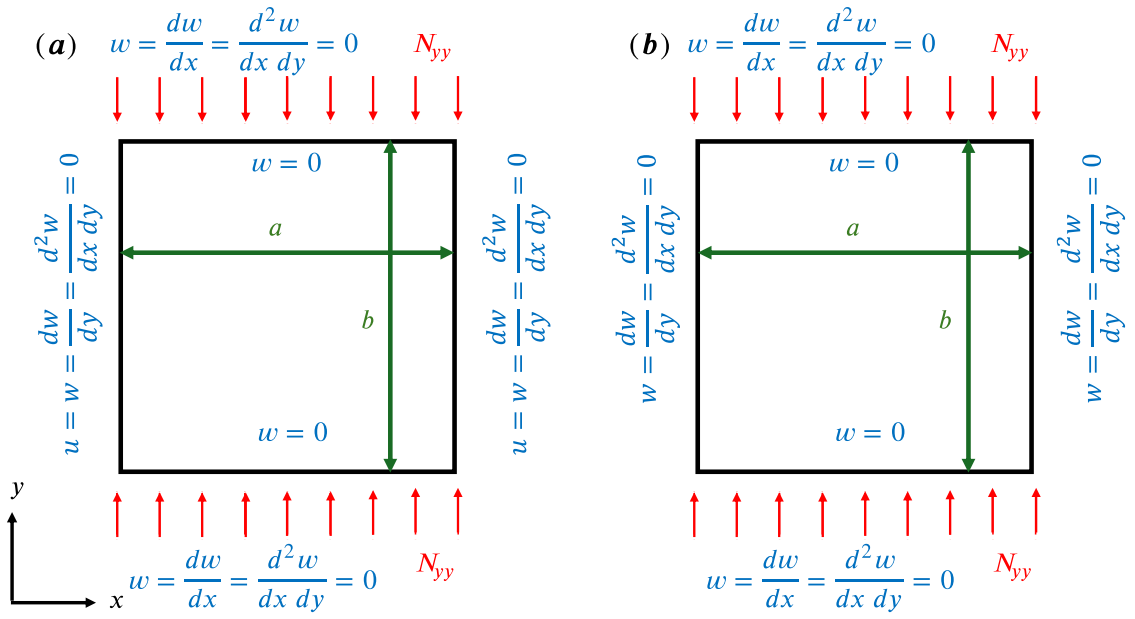


Fig. 2. Plate geometry, in-plane loads by (a) simply supported with constrained lateral edges (SSSS-Lateral Constrained) and (b) simply supported with free lateral edges boundary conditions (SSSS-Lateral Free).

Table 1
Mechanical properties of unidirectional lamina used in the Refs. [31,47,53–55]. The direction in the subscripts: '1' indicates the fiber axis and '2' is the transverse direction to the fiber axis in the lamina plane.

E_1	ν_{12}	E_2	G_{12}	$G_{23} = G_{13}$
181 GPa	0.28	10.273 GPa	7.1705 GPa	2.6 GPa

buckling load ($F_{cr} = \lambda_1 R_y$) instead of maximizing the load ratio (λ_1). The reaction force along y-direction, R_y, is the sum of the membrane reaction normal force, p_{myy}, along the bottom/top edge of the plate which has a length of a:

$$R_y = \frac{1}{a}\int_0^a p_{myy}\,\mathrm{dx}. \tag{49}$$

3. Validation

The in-house finite element code was performed to calculate the critical buckling load to make numerical and experimental comparisons with the findings of the literature.

3.1. Numerical

Two validation cases are selected according to Ref. [56]: **i.** a plate with simply supported edges with constrained lateral edges and **ii.** a plate with simply supported edges and free lateral edges. The in-plane load is applied vertically and the optimal cases are studied (Fig. 2). The two plates have dimensions of 254 mm × 254 mm (ratio = 1) and total thickness of 1.524 mm. The mesh convergence is studied and the mesh resolution of 13 × 13 is chosen with convergence of 0.67% with respect to the finer meshes.

The material properties are according to Table 1. The first buckling factors λ_1 and the resulting buckling loads are calculated for both cases. As shown in Table 2, layup designs studied for each case include Quasi-Isotropic (QI), optimum constant stiffness (CS) and optimum variable stiffness (VS) plates.

The conventional layup of $[\pm 45/0/90]_s$ is chosen as the QI laminate instead of the zero lamination parameters according to Ref. [56]. The optimum CS plate is designed to be a symmetric four-layer laminate to compare with the resource data. The results have a good fit, and small deviations arise from element differences and their formulations. The buckling factor is nondimensionalized according to $\lambda_{cr} = \lambda N_{cr} a^2/(E_1 h^3)$. The resulting critical buckling force, F_{cr}, is calculated with $F_{cr} = \lambda_{cr} a N_{yy}^{av}$.

The optimization outcomes demonstrate remarkable similarity, with a maximum deviation of 3.5%, thereby affirming the methodology employed, as shown in Table 2. The deviations are due to a combined effect of differences in the element type and optimization method.

3.2. Experimental

An experimental validation is carried out using the recent findings in [57,58]. The mechanical properties of the material used here are given in Table 3.

The buckling test fixture used in [57,58] consists of rigid knife-edge supports that prohibit out-of-plane displacement and allow tangential rotation. In order to make the lateral edges move freely, a 2 mm gap was left between the supports and the vertical edges of the composite plate. In order to satisfy this condition, the geometry and boundary specifications used here are according to Fig. 2.b, in which the edges are fully simply supported with free lateral edges.

The dimensions of the plate are a = 254 mm and b = 406 mm and the total thickness is t = 2.47 mm. The layup design used in the reference includes the quasi-isotropic case, variable stiffness design with complete overlaps (no gap), and variable stiffness design with complete gaps (no overlap). The VS design has an overall constant radius of curvature of r = 625 mm as in [57,58]. Due to fiber overlaps and gaps, thickness variation occurs throughout the plate, and fiber gaps cause thickness reduction, while fiber overlaps lead to an increase in the thickness. The load is applied vertically in the form of uniaxial compression and lateral expansion is allowed for vertical edges. The buckling condition is simulated with a mesh with 11 by 13 elements along x and y directions, respectively, and mesh convergence is satisfied with the mentioned resolution of the edges.

Table 4 shows the results of the current study comparing to the experimental and numerical results of [57,58]. The results of the current study without the application of the curvature constraint ($\alpha = 0$) is the ideal case, gives the maximum stiffness for the buckling load. As experimental studies have applied steering of tow fibers with a

Table 2
Comparison between results of current study and results of T. IJsselmuiden [56] for two cases. First case is a plate with SSSS, fully simply supported edges (out-of-plane BCs), and lateral edges constraints (in-plane BCs). Second case is a plate with SSSS, fully simply supported edges (out-of-plane BCs), and lateral edges free (in-plane BCs).

Laminate	Layup	Out-of-plane BCs	In-plane BCs	F_{cr} (kN)	λ_1 (current study)	λ_1 (IJsselmuiden)	dev%
QI	$[\pm 45/0/90]_s$	SSSS	Lateral Constrained	2.76	1.09	1.0597	2.9%
Optimum CS	$[\pm 28]_s$	SSSS	Lateral Constrained	3.11	1.23	1.1885	3.5%
Optimum VS	–	SSSS	Lateral Constrained	6.16	2.44	2.4692	1.2%
QI	$[\pm 45/0/90]_s$	SSSS	Lateral Free	3.57	1.42	1.3734	3.4%
Optimum CS	$[\pm 45]_s$	SSSS	Lateral Free	4.49	1.78	1.7316	2.8%
Optimum VS	–	SSSS	Lateral Free	8.83	3.5	3.4773	0.7%

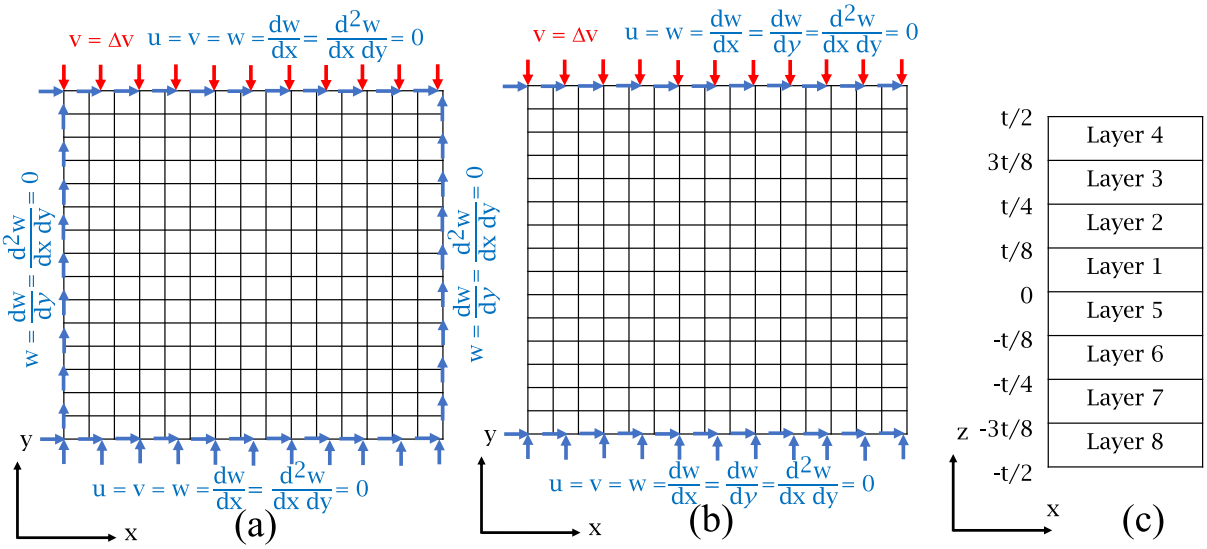


Fig. 3. Mesh with (a) clamped–clamped–free–free (CCFF) in-plane and clamped–clamped-simply supported-simply supported (CCSS) out-of-plane boundary conditions (BCs), (b) CCFF in-plane and CCFF out-of-plane BCs, and (c) layup sequence for eight layers. The angle of the fiber is measured with respect to the x-axis, the loading was along the y-axis, and the laminate has a total thickness of t along the z-axis.

Table 3
Mechanical properties of unidirectional lamina used in the Refs. [57,58].

E_1	ν_{12}	E_2	G_{12}
142.7 GPa	0.3	9.1 GPa	4.82 GPa

constant radius of r = 625 mm, the current research applies the LSC method and the curvature constraint of the same radius to compare the results. A close match for the critical load results is obtained when considering the curvature constraint. The deviation in the results from the experiments is due to the imperfections that were introduced during the plate manufacturing, which is unavoidable. Uncontrolled gaps and overlaps without a specific criterion were observed to limit them, and other manufacturing defects combined with autoclaving of the composite plate were observed to intensify this deviation. For example, the two different sets of experiments carried out by the same authors did not reveal the same force-displacement response. In the current study, the application of LSC with curvature constraint is based on the no-gap condition and matches the no-gap results of [57,58]. For this reason, the deviation is computed in terms of percent difference from the critical load after applying the curvature constraint, and the reason is discussed here. Another important reason even for deviation of QI layup, which is a constant stiffness case, is that the authors were not steadfast in the selection of the thickness of the plate under study, which considerably affects the final results. We have taken the total thickness of the plate equal to the number of plies times the thickness of each tow fiber to have consistency in our study which was not clear in the reference studies. It seems that they have manufactured and then measured the thickness, and then applied to the simulation which will make deviation from our study. A similar issue arises when the constant steering radius was used throughout the plate, which is different from the current study. This paper adopts the threshold radius (r = 625 mm) as the minimum value required to prevent distortion or wrinkling of the tow fiber. However, it is not necessary for this value to remain constant across the entire plate. Applying a greater number of constraints to fiber steering causes a larger deviation from the true optimal outcomes. All of these led to a deviation of 11.4% scatter in the own results of the references.

To summarize, in light of the previously noted manufacturing defects and methodological differences, the current study's deviation of 2.2% from one experimental finding for the VS optimum plate offers a dependable insight into the existing formulations.

4. Results

Design optimization was performed for plate compression buckling. In general, the boundary conditions for a plate are either clamped or simply supported edges for buckling simulations [31,47,53–55]. However, in practice, it is quite challenging to satisfy simply supported boundary conditions at the edges of a plate during compression. The two opposite ends of the plates at the top and bottom of the plate restricted both in-plane and out-of-plane displacements at the top and bottom edges of the plate, while the remaining two edges are free. Plate compression was applied in the form of both displacement and force boundary conditions in the upper nodes, as shown in Fig. 3.

In some references, displacement boundary conditions are employed [31,53] but our formulation is based on optimizing the critical buckling ratio λ_1, which assumes constant reaction forces. Otherwise,

Table 4
Comparison of critical buckling loads (F_{cr}) across different experimental and numerical studies and deviation percent of the reference loads from the current study after applying curvature constraint (F^*_{cr}) [57,58].

Layup	$F_{cr}(kN)$ (current study, $\alpha = 0$)	F^*_{cr}(kN) (current study , $\alpha \neq 0$)	$F_{cr}(kN)$ [dev*%] Exp. [58]	$F_{cr}(kN)$ [dev*%] Exp. [57]	$F_{cr}(kN)$ [dev*%] Num. [57]
QI	12.7	12.7	11.52 [10.2%]	11.52 [10.2%]	13.08 [2.9%]
VS (gap)	–	–	12.19	12.32	13.52
VS (overlap)	28.44	18.55	18.97 [2.2%]	20.8 [10.8%]	21.14 [12.3%]

Table 5
Optimization results for constant stiffness (CS) laminates: critical load ratio (λ_1), total reaction force (R_y), critical buckling load (F_{cr}), lamination parameters (ξ^i_j), and the corresponding layup sequence for uniform lamina layer thickness.

Laminate:	$\lvert\lambda_1\rvert$	$\lvert R_y \rvert$ [kN]	$\lvert F_{cr}\rvert$ [kN]	ξ^A_1	ξ^A_3	ξ^D_1	ξ^D_3	Layup
Optimum (CS)	0.0857	13.32	1.142	0.7330	0.1062	0.6208	−0.2580	≃[[23/−23/S]/A]
Transversely iso. (CS)	0.0231	72.64	1.678	0	0	0	0	≃[[63/−63/S]/A]
Conventional (CS)	0.0171	97.53	1.667	0	1	0	1	[[90/0/S]/A]
Conventional (CS)	0.0383	35.02	1.341	0	−1	0	−1	[[45/−45/S]/A]
Unidirectional (CS)	0.0141	184.24	2.598	−1	1	−1	1	$[90]_8$
Unidirectional (CS)	0.0504	10.44	0.527	1	1	1	1	$[0]_8$

Table 6
Absolute values of the critical buckling load ratio (λ_1), membrane reaction force (R_y), and critical buckling force (F_{cr}) for different cases for VS design: transversely isotropic (iso.), after optimization in terms of the lamination parameters (opt.) with ($\alpha = 100$) and without ($\alpha = 0$) the interpolation of lamination parameters, and after conversion of lamination parameters to angles (ang.) for $\alpha = 100$.

	iso. (CS)	opt. (CS)	opt. $\alpha = 0$ (VS)	opt. $\alpha = 100$ (VS)	ang. $\alpha = 100$ (VS)
$\lvert\lambda_1\rvert$ [–]	0.0231	0.0857	0.1362	0.1301	0.1116
$\lvert R_y\rvert$ [kN]	72.64	13.32	22.203	22.855	20.167
$\lvert F_{cr}\rvert$ [kN]	1.678	1.142	3.025	2.974	2.270

the optimization method must be modified to optimize the critical buckling load, F_{cr}, instead of the buckling load factor. The mesh convergence revealed a discretization of a square plate with 15 elements per edge, resulting in a finite element mesh containing 225 total elements A. Linear isoparametric elements and Bogner–Fox–Schmit type elements were used for the in-plane and out-of-plane degrees of freedom, respectively.

Optimal tow angles and layup sequences were obtained using the proposed optimization method. The method is developed for specially orthotropic cases that correspond to antisymmetry that is applied to a balanced half-laminate. The setup sequence had eight layers with each layer 0.16 mm thick. Fig. 3(b) shows the numbering of layers used in this study. Fiber angles were defined with respect to the x-axis shown in Fig. 3. In the case of force boundary conditions, the input displacements, $v = \Delta v$, which are indicated in red color in Fig. 3(a) and (b) are suppressed, and are replaced instead with a distributed edge load; this is not shown in the figure for clarity.

Optimization was performed for different cases, including plates with constant stiffness (CS) and variable stiffness (VS). The lamination parameters remain constant throughout the domain for the CS case, while the lamination parameters for every element vary for the VS case.

4.1. Constant stiffness optimization

The mesh with 225 elements and with CCFF-SSSS boundary conditions as shown in Fig. 3(a) is used for in-plane and out-of-plane displacements, respectively. Optimum refers to the optimum solution that is obtained right after optimization before conversion of the lamination parameters to reveal a stacking sequence. The transversely isotropic solution refers to the configuration at the origin of the lamination parameter space ($\xi^A_1 = \xi^A_3 = \xi^D_1 = \xi^D_3 = 0$). The conventional layout sequence refers to the specially orthotropic configuration using conventional laminates such as [90°/0°/0°/90°/A] or [±45°/∓45°/A]. The non-conventional result is the specially orthotropic configuration [[±θ/S]/A] for an angle within the range of [90°,−90°) θ with a minimum of eight layers[4].

Table 5 shows the optimization results for different CS cases. Optimization results in a CS plate with 124% better critical load ratio than the best conventional CS case ([[45/-45/S]/A]) revealing the performance of optimization. However, the critical buckling load of the optimum CS case, $\lvert F_{cr}\rvert$, is lower than that of the conventional UD laminate. This is related to the use of displacement boundary conditions (Diriclet) as inputs in the form of uniform edge shortening.

4.2. Variable stiffness optimization

The in-house code is used to obtain the optimal lamination parameters and the buckling response, $|\lambda_1| = 0.1301$ for $\alpha = 100$ from Table 6. Optimization reveals a load ratio of approximately 160% higher for the VS design compared to the optimum CS case. Similarly, the result is 563% higher than that of the transversely isotropic case. In addition, the result is nearly 400% higher than that of the closest orthotropic conventional laminate consisting of layers of 0°/90° fiber angles. However, the gain in critical buckling load are much less.

Fig. 4 shows the distribution of the optimal lamination parameters. The distributions resemble the findings in the Refs. [31,55] but rotated 90° due to the difference in the compression direction. Although the type of finite elements in those references is quite different than in the present study, the lamination parameters have a fairly similar distribution. But, for example in [47] we had a different scale bar for each plot, making comparison difficult. Both in-plane and out-of-plane lamination parameters have four-fold symmetric distributions, which validates the approach used. The iterations started from the center of the feasible space to guarantee that the lamination parameters start within a feasible domain. A similar pattern was obtained if the feasible randomly generated initial values of lamination parameters were used instead.

[4] In the laminate representation [S/A], 'S' and 'A' stand for symmetric and anti-symmetric laminate.

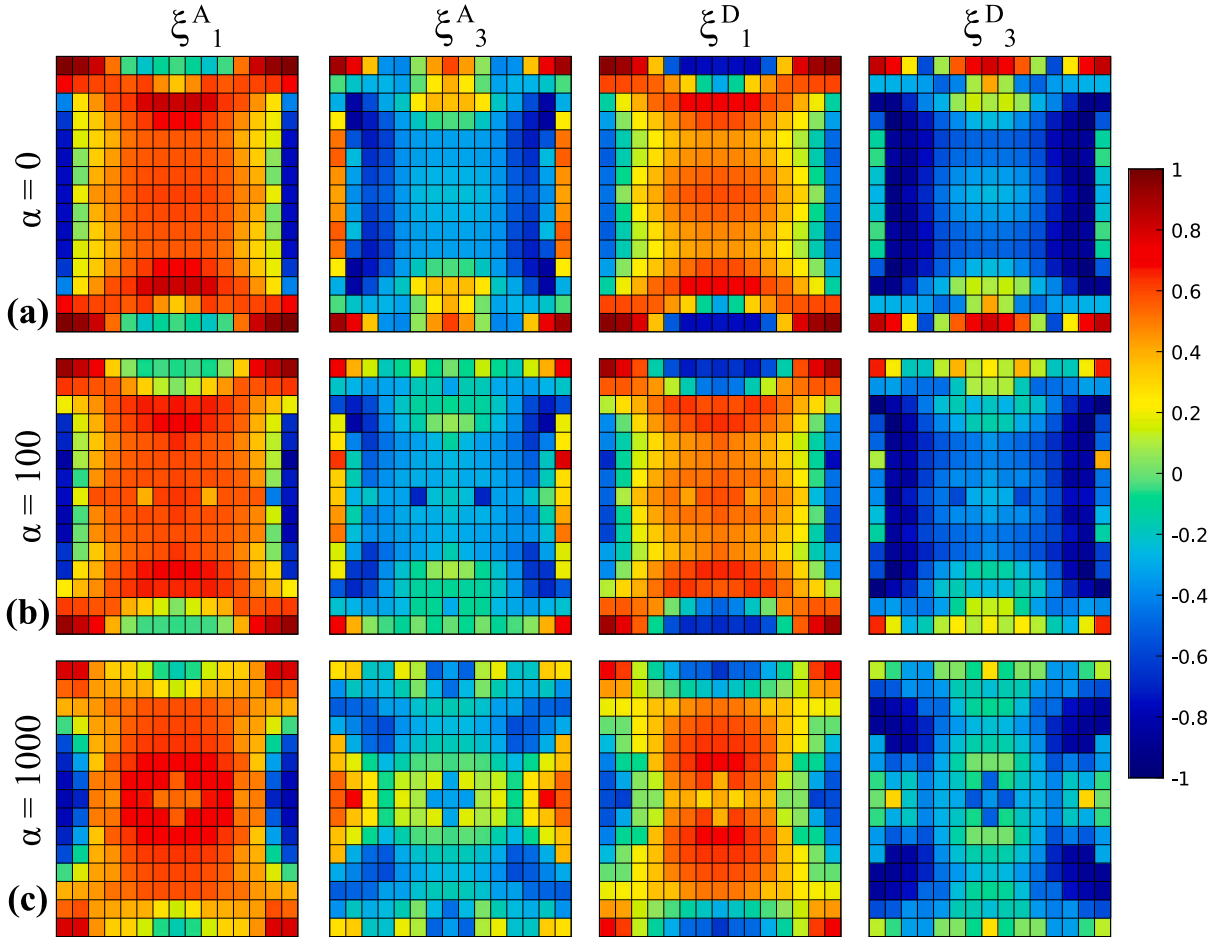


Fig. 4. Optimum lamination parameter distribution for CCFF in-plane and SSSS out-of-plane boundary conditions. The penalty parameters, α, are: (a) 0, (b) 100, and (c) 1000.

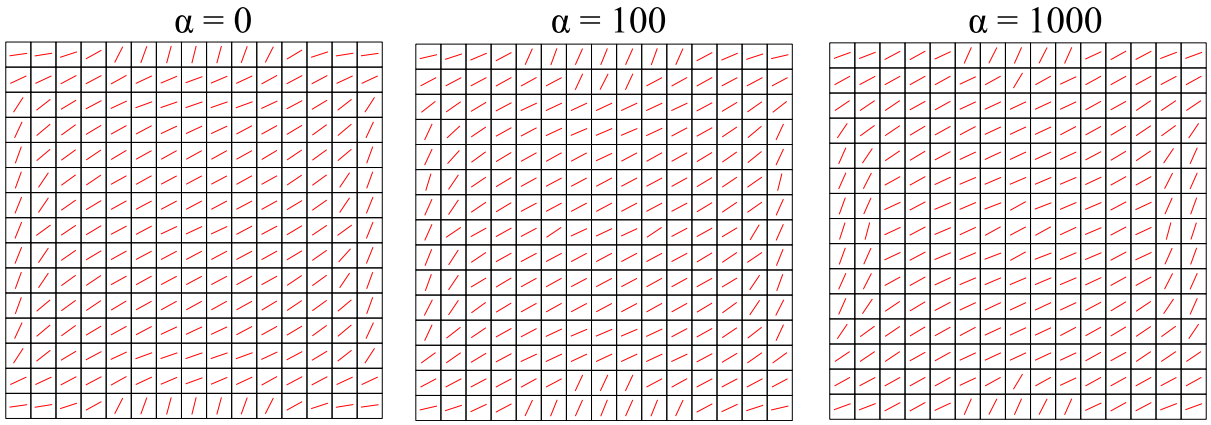


Fig. 5. Optimum fiber angle distributions on the first layer after conversion of lamination parameters to fiber angles corresponding to the penalty parameter, α, of 0, 100, and 1000. The angles in the remaining layers of the eight-layer specially-orthotropic laminate have either the same or the anti-symmetric distribution [$\pm\theta/\mp\theta$/A], hence not shown. The plate had 15 elements per edge and the in-plane, the input load was of displacement type, and out-of-plane boundary conditions were CCFF-SSSS, respectively.

The conversion of the lamination parameters to the fiber angles in Fig. 5 reveals that the fiber or tow angles are continuous to a certain degree. Fig. 6 shows the decreasing value of the maximum curvatures as the penalty parameter increases. The same penalty parameter was used throughout the layers because the angles on a single layer define that in the rest of the layers for a specially orthotropic laminate consisting of eight layers.

The elemental variation of the curvature is calculated for the selected penalty parameters as shown in Fig. 6. The curvature distribution is the same for the remaining layers and is therefore not shown. The maximum value of the curvature is 0.022 mm^{-1}, 0.020 mm^{-1} and, 0.018 mm^{-1} for the corresponding penalty factors of 0, 100, and 1000, respectively. The curvature decreases as the penalty factor increases, but the interpolation increases the number of optimization iterations (approximately 3 × more computational time for $\alpha = 100$ compared to $\alpha = 0$), which hinders the efficacy of the optimization. Therefore, $\alpha = 100$ compromises the maximum curvature, while allowing optimization

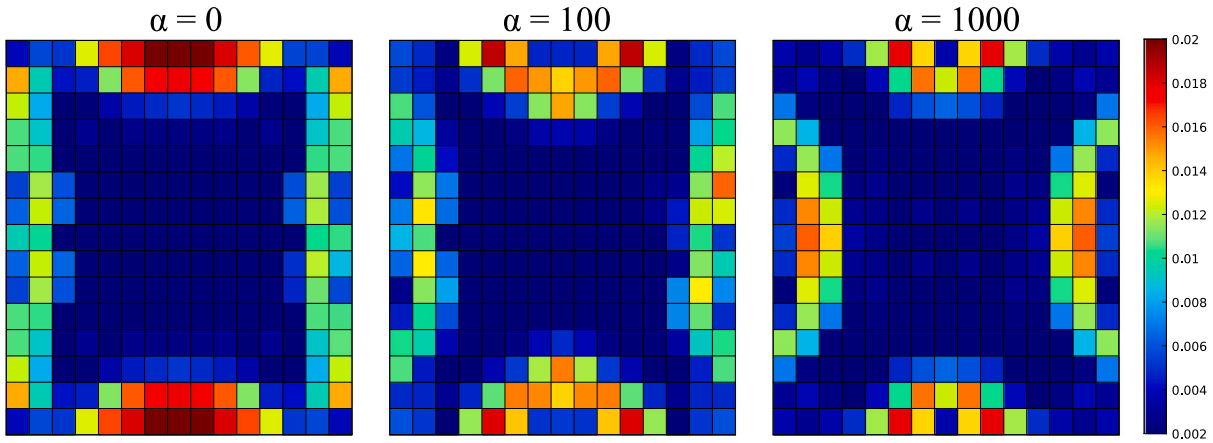


Fig. 6. Maximum curvature distribution on the first layer of the laminate for the penalty parameters of $\alpha = 0$, $\alpha = 100$, and $\alpha = 1000$ (left to right). The remaining layers of the eight-layer specially-orthotropic laminate, $[[\pm\theta/S]/A]$, has a similar distribution, hence not shown. The plate had 15 elements per edge and the in-plane, the input load was of displacement type, and out-of-plane boundary conditions were CCFF-SSSS, respectively.

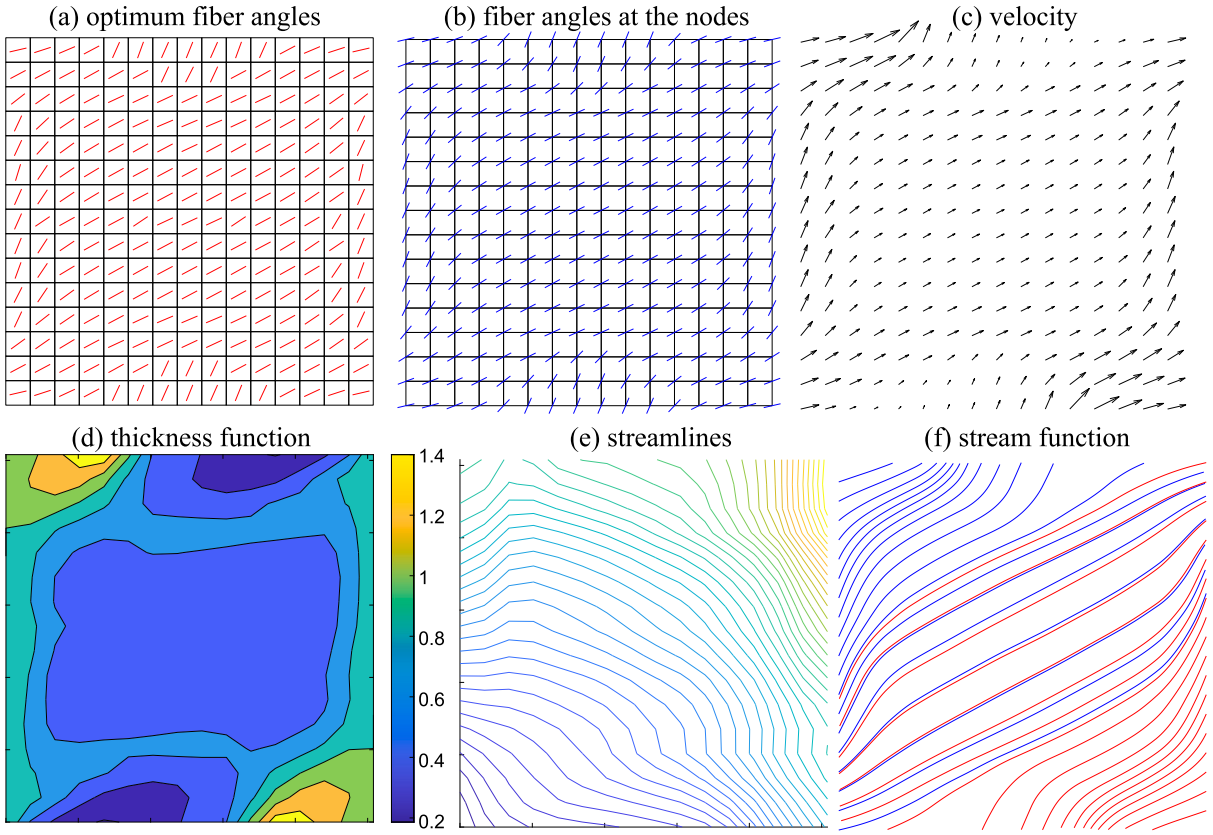


Fig. 7. Optimization results after the stream function analysis on the first layer of the laminate: (a) optimum fiber angles, (b) fiber angles at the nodes, (c) velocity, (d) thickness function, (e) streamlines, and (f) stream function plots. The plate had 15 elements per edge, the optimization penalty parameter was $\alpha = 100$, the input load was of displacement type, and the in-plane and out-of-plane boundary conditions were CCFF-SSSS, respectively.

to be completed in a reasonable computational time. In addition, the resulting curvature is not much different from the case with $\alpha = 1000$ except for the maximum curvature, Fig. 6.

The application of constraints in conjunction with optimization of the lamination parameter reveals continuous and manufacturable fiber-tow angle distributions. The fiber angle distributions corresponding to the penalty factor $\alpha = 100$ in Fig. 6 reveal continuous fiber angle distributions that satisfy the curvature limits. This can be concluded by assuming that the local sharp changes of curvature will further be filtered through the streamline approach and disappear in the final angle distributions.

Table 6 shows the first buckling load factor, λ_1, reaction force, R_y, and critical buckling load, F_{cr} for the VS design and its comparison to various CS designs. The optimized buckling load decreases by 1.7% after conversion of the lamination parameters to the fiber angles. In order for the plate to be manufactured with optimum fiber angles, F_{cr}

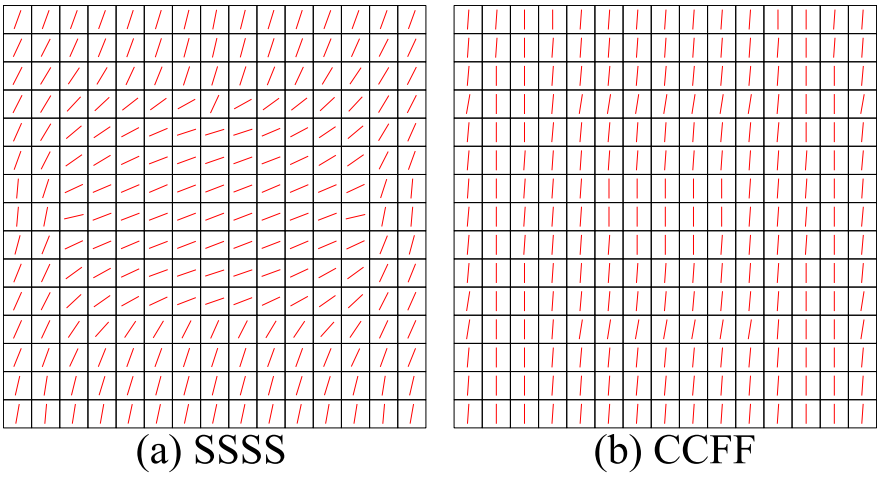


Fig. 8. The fiber angles in the first layer obtained by using different loads of (a) force and (b) displacement as the input. The plate had 15 elements per edge, the penalty parameter for the optimization was $\alpha = 100$, the force input was used the load, and the in-plane and out-of-plane boundary conditions were CCFF-SSSS, respectively.

Table 7
Absolute values of the critical buckling load ratio (λ_1), membrane reaction force (R_y), and critical buckling force (F_{cr}) for different out-of-plane fixtures: simply-supported (SSSS) and clamped-clamped-free-free (CCFF).

	SSSS	CCFF
$\lvert\lambda_1\rvert$ [–]	13.386	9.719
$\lvert R_y\rvert$ [kN]	0.254	0.254
$\lvert F_{cr}\rvert$ [kN]	3.400	2.469

Table 8
Absolute values of the critical buckling load ratio (λ_1), membrane reaction force (R_y), and critical buckling force (F_{cr}) for different boundary conditions: displacement and force. The results are obtained by using penalty factor, α, of 100, for the mesh with 15 elements per edge, and for the lamina properties in Table 1.

	Diriclet (disp.)	Neumann (force)
$\lvert\lambda_1\rvert$ [–]	0.1301	13.386
$\lvert R_y\rvert$ [kN]	22.855	0.254
$\lvert F_{cr}\rvert$ [kN]	2.974	3.400

is compromised with an acceptable value. Angles exceeding the curvature limit are expected to become less after the streamline analysis. Obviously, the higher enforcement of curvature constraint reduces the objective function, as expected, which in the extreme situation, the solution converges to the optimum CS case.

The stream function analysis converts the discrete angles into paths to allow the manufacture of the designed plates. AFP manufacturing platform uses these splines as guide curves to steer the tows. Therefore, for VS design cases, the tow angles are obtained by applying stream function analysis to the optimum fiber angles. Fig. 7 shows the results of the stream function analysis used in this study: (1) the optimal fiber angles are calculated inside the elements, (2) these angles are then extrapolated to the nodes using the shapes functions of the membrane, (3) the angles are expressed in terms of velocity components, (4) the stream functions are used with velocity as input to obtain the thickness function, streamlines, and stream functions.

Fig. 7(f) shows the streamlines obtained for the VS case for the penalty factor of $\alpha = 100$. The two colors indicate the stream lines that start at the two opposite ends of the plate. For example; the stream lines in blue color initiate from the left edge of the plate while the streamlines in red color initiate from the right edge. The use of a top-bottom or left–right edge as the path start-end locations is decided on the average of the overall angle distribution. If the mean angle is within the range $\pm 45°$, the left and right edges were used at the starting edges of the stream lines; and the top and bottom edges are used otherwise.

4.3. Ideal (SSSS) versus practical (CCFF) out-of-plane fixtures

The effect of the ideal and practical out-of-plane boundary conditions is investigated. It is practically difficult to achieve zero out-of-plane displacements at the edges of the plate for the ideal simply supported boundary conditions (SSSS) for plate compression. Special fixtures are necessary to achieve this condition. It is more likely to achieve two opposite edges on one of which the load is applied fully clamped while the two edges remain free (CCFF).

Table 7 shows the optimization results for different out-of-plane boundary conditions. The force input boundary condition (Neumann type) was used for both cases. The ideal SSSS out-of-plane boundary conditions reveal a 38% better critical buckling load than that of the practical CCFF boundary condition.

Fig. 8 shows the optimum distribution of the fiber angles for the out-of-plane boundary conditions of SSSS and CCFF. The input load was in the form of force (Neumann-type) to illustrate the effect of input boundary conditions with more precision. Fiber angles had a complex distribution when SSSS type boundary conditions were used, Fig. 8(a). However, under uniform force loading, the fibers tend to align themselves with the load, Fig. 8(b). This reduces both the load ratio and the critical buckling load.

4.4. Input load as Diriclet (displacement) or Neumann (force) boundary condition

The effect of the type of input boundary condition is investigated. The value of the input boundary condition was unity (1 mm or 1 kN/mm) for both cases. The mesh with 15 elements per edge and penalty factor α, of 100 is used in the simulation with the material properties shown in Table 1. The in-plane and out-of-plane boundary conditions were CCFF-SSSS, respectively.

Table 8 shows the results of the optimization for VS design. The critical buckling load decreases by 12.5% when the displacement input or uniform edge shortening was used as the boundary displacement input.Fig. 9 shows the optimum fiber angle distributions. However, fiber angles are more clustered when force boundary conditions were used as input, with a higher deliverable of the critical buckling load. The boundary conditions are very important for the solution.

The optimization method is formulated assuming constant reaction forces, which is fulfilled when force inputs are used. However, the reaction forces do not remain constant during optimization when displacement boundary conditions are used. Therefore, the objective

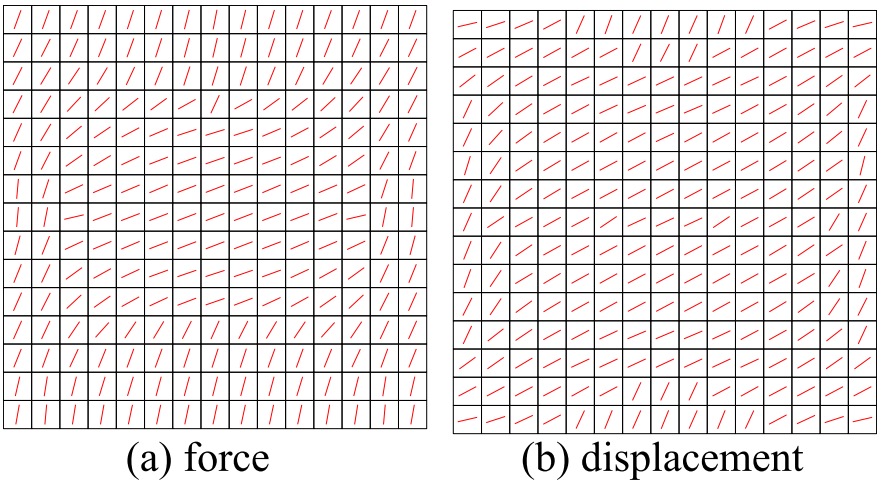


Fig. 9. The fiber angles in the first layer obtained by using different types of boundary conditions for the inputs: (a) force (Neumann) or (b) displacement (Diriclet). The plate had 15 elements per edge, the penalty parameter for optimization was $\alpha = 100$, and the boundary conditions in and out of the plane were CCFF-SSSS, respectively.

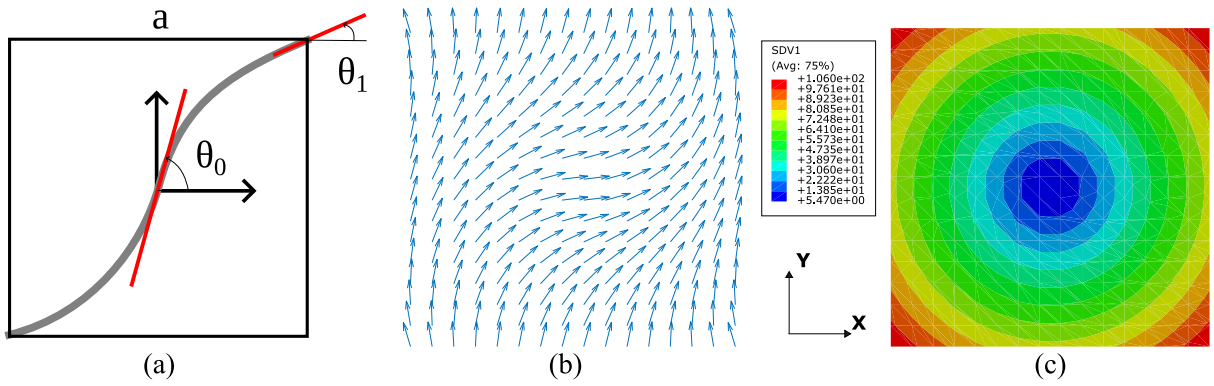


Fig. 10. Optimum fiber angle distributions for plate compression buckling according to [46] and Eq. (50): (a) schematic sketch of linear angle variation with parameters θ_0 and θ_1, (b) at the nodes in Matlab® for $\theta_0 = 0$ and $\theta_1 = 75°$, (c) at the integration points in Abaqus®-UMAT for $\theta_0 = 0$ and $\theta_1 = 75°$.

function shall be the critical buckling load, which is obtained by multiplying the critical buckling load ratio by the total membrane reaction force. Although this is a simple fact, it was overlooked in many references, hence it is investigated.

4.5. A widely-accepted optimal fiber angle distribution [46]

The optimum distribution of the fiber angles proposed in Ref. [46] has been widely accepted. In this section, we implement a material model in the user-subroutine (Abaqus®-UMAT) to define variable stiffness for each element and the integration point. Buckling analysis and quasi-static analysis are performed on the plate with varying fiber angle distribution separately to obtain eigenvalues and membrane reactions, respectively. Comparison of the VS plate with two different CS cases was performed to clearly understand the deliverables. As a reminder, optimization was not performed in this section; the objective is to compare the buckling response obtained from the suggested optimum angle distributions in [46] to CS cases with simple buckling and quasi-static analyses using the same computational environment (Abaqus®-UMAT).

The optimum buckling response is obtained for the linear variation of the fiber angles obtained by Eq. (50) in which θ_0 and θ_1 represent the fiber angles in the center and at the end of the plate, respectively. Angles are measured with respect to the angular position of the reference point ϕ, which is taken to be zero in this case. The parameter a represents the edge length of the square plate [46]:

$$\theta(\mathbf{x}) = \phi + \frac{\theta_1 - \theta_0}{a/2} \|\mathbf{x}\| + \theta_0. \tag{50}$$

The maximum normalized critical load ratio was 3.14 when θ_0=0° and θ_1=75° with respect to the loading axis (the loading axis was along x-direction in [46]) for CCFF-SSSS in-plane and out-of-plane boundary conditions. The material parameters were the same as in Table 1. Fig. 10 shows the fiber angle distribution as that given in Eq. (50). Fig. 10(b) shows the distribution of the fiber angles according to Eq. (50) calculated for each node in Matlab®. The same angles are computed within Abaqus®-UMAT and exported as a state dependent variable (SDV-1) as shown in Fig. 10(c). The two plots are consistent with each other.

In order to define the variable fiber angles different for each element as shown in Eq. (50), the UMAT user-defined material subroutine was used within Abaqus®. The input files and the code are available at https://github.com/EralpDemir/Composite-Materials [52]. The input files of the models for buckling analysis and static analysis are also provided on the same link.

Lamina stiffness needs to be transformed for each element and for each integration point using for any fiber angle, θ, the lamina stiffness transformations according to:

$$\begin{aligned}
\overline{Q}_{11} &= \cos\theta^4 Q_{11} + \sin\theta^4 Q_{22} + \cos\theta^2 \sin\theta^2 (2Q_{12} + 4Q_{66}),\\
\overline{Q}_{12} &= \cos\theta^2 \sin\theta^2 (Q_{11} + Q_{22} - 4Q_{66}) + (\cos\theta^4 + \sin\theta^4) Q_{12},\\
\overline{Q}_{16} &= \cos\theta^3 \sin\theta (Q_{11} - Q_{12} - 2Q_{66}) + \cos\theta \sin\theta^3 (Q_{12} - Q_{22} + 2Q_{66}),\\
\overline{Q}_{22} &= \sin\theta^4 Q_{11} + \cos\theta^2 \sin\theta^2 (2Q_{12} + 4Q_{66}) + \cos\theta^4 Q_{22},\\
\overline{Q}_{26} &= \sin\theta^3 \cos\theta (Q_{11} - Q_{12} - 2Q_{66}) + \cos\theta^3 \sin\theta (Q_{12} - Q_{22} + 2Q_{66}),\\
\overline{Q}_{66} &= \cos\theta^2 \sin\theta^2 (Q_{11} + Q_{22} - 2Q_{12} - 2Q_{66}) + (\sin\theta^4 + \cos\theta^4) Q_{66}.
\end{aligned} \tag{51}$$

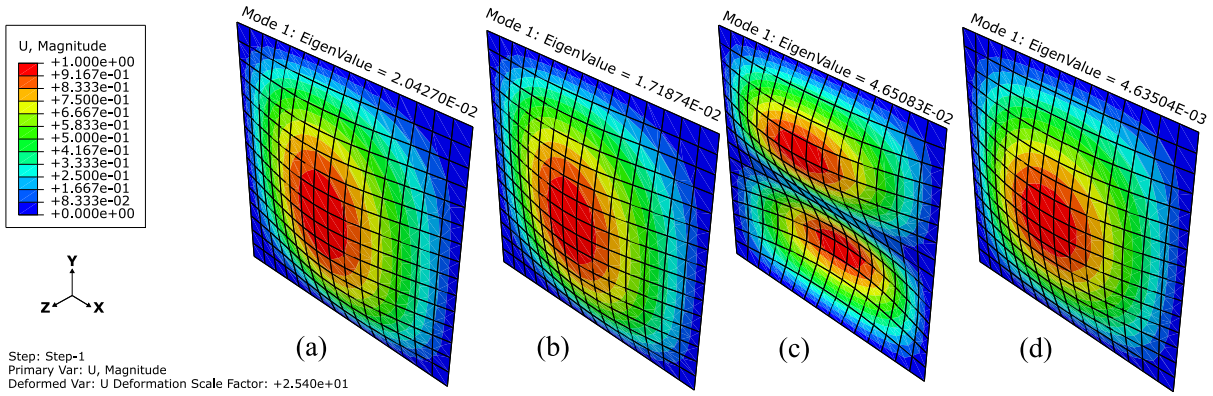


Fig. 11. First mode shapes and critical buckling load ratios obtained using Abaqus®-UMAT for VS design in [46] of a (a) single layer (θ), (b) symmetric two layers ($\theta/-\theta$) (c) CS-UD with 0°, and (d) CS-UD with 90°. 0° refers to fibers being along the x-direction.

Table 9
Inputs to UMAT using PROPS vector. E_{11}, E_{22}, ν_{12}, and G_{12} are the elastic properties of the lamina. θ_0, θ_1, and ϕ are the angular parameters in Eq. (50). a and t are the width and the total thickness of the plate. PROPS(10) is a flag to indicate whether it is an in-plane or out-of-plane analysis, needed because stiffness matrices are different for the two cases.

PROPS()	Property	Unit
1	E_{11}	MPa
2	E_{22}	MPa
3	ν_{12}	–
4	G_{12}	MPa
5	θ_0	deg.
6	θ_1	deg.
7	ϕ	deg
8	a	mm
9	t	mm
10	1 or 0	–

The reduced stiffness matrix, $\overline{\mathbf{Q}}$, is obtained by substituting the components:

$$\overline{\mathbf{Q}} = \begin{bmatrix} \overline{Q}_{11} & \overline{Q}_{12} & \overline{Q}_{16} \\ \overline{Q}_{12} & \overline{Q}_{22} & \overline{Q}_{26} \\ \overline{Q}_{16} & \overline{Q}_{26} & \overline{Q}_{66} \end{bmatrix}. \tag{52}$$

The user material subroutine demands for two main definitions; stress and the material tangent. The stiffness of the lamina, $\overline{\mathbf{Q}}$, is used as the tangent stiffness matrix (DDSDDE), and the corresponding stress (STRESS) is computed from the given strain increments. The code is written for small strain cases, which is defined by the user. Similarly, the properties of the user-defined material are transferred to UMAT by a vector (PROPS) that contains ten inputs that are described in Table 9. PROPS(10) is used as a flag to indicate whether the analysis is in-plane (with a value of "1") or out-of-plane (with a value of "0"). The state variable vector (STATEV) is used to visually show the fiber angles that are different for each element in the VS case. More details on how to generate the finite element model can be found in [59].

Fig. 11 shows the critical (first) buckling mode corresponding to different fiber angles of Fig. 11(a) VS with angle distribution in Eq. (50), Fig. 11(b) CS with 0° UD, and Fig. 11(c) CS with 90° UD. The material parameters are the same as in Table 1 and the thickness is the same as the laminate thickness. Uniform end shortening as Diriclet boundary condition is used as input load as used in [46] for consistency. In addition to buckling, a quasi-static in-plane analysis is performed to obtain membrane reaction forces.

Table 10 shows the load ratio, total membrane reaction forces, and critical load obtained for the three cases. The case 90° reveals the highest critical buckling load when the fibers are aligned vertically along the loading direction rather than steering with the suggested angles according to (50).

Table 10
Absolute values of the critical buckling load ratio (λ_1), membrane reaction force (R_y), and critical buckling force (F_{cr}) for variable-stiffness (VS) design in [46], and constant stiffness (CS) designs with 0° and 90° fiber angles. The results are obtained by using Abaqus®-UMAT using a mesh with 15 elements per edge, and for the lamina properties in Table 1.

	VS (θ) [46]	VS ($\theta/-\theta$) [46]	CS - 0°	CS - 90°
$\lvert\lambda_1\rvert$ [–]	0.0204	0.0172	0.04651	0.00464
$\lvert R_y\rvert$ [kN]	38.365	20.420	10.609	187.62
$\lvert F_{cr}\rvert$ [kN]	0.790	0.351	0.493	0.882

The direction of the fiber angles as suggested in the Ref. [46] for the case with two clamped ends and two free edges for a compression buckling case (a single layer with $\theta_0 = 0°$ and $\theta_1 = 75°$ for case B) gives the critical load ratio of $\lambda_1 = 0.0206$ with a critical load of $\|F_{cr}\| = 0.790$ kN. However, $\lambda_1 = 0.0047$ and $\|F_{cr}\| = 0.882$ kN for straight fibers aligned with the loading axis (CS 90°). The VS design gives a better solution compared to the unidirectional case (UD) CS with a fiber angle 0°, but it does not reveal a better solution than the UD case CS with a fiber angle 90°. The CS UD case with the 0° fiber angle reveals a higher order mode shape with a higher critical load ratio but much lower membrane reaction forces due to the lowest possible stiffness along the loading direction. Therefore, the best buckling performance is obtained by the UD lamina with fiber directions aligned along the loading direction.

5. Conclusions

The buckling optimization technique was effectively applied to determine the optimal arrangement of lamination parameters and fiber orientations to achieve the highest critical load ratio. The validation of the code is performed both numerically [56] within 0.7–3.5% variation for different design cases and experimentally [57,58] within approximately 2.2–10.8% deviation which is within the experimental scatter. The application to compression buckling case leads to the following important conclusions:

- The proposed optimization method revealed an increase in the optimum buckling load (F_{cr}) for a variable stiffness case to be 160% more than compared to an optimum constant stiffness case. The improvement in the critical load ratio (λ_1) was greater than approximately 400% relative to the quasi-isotropic case, which is consistent with the literature findings [31,46].

- Employing lamination parameters as a field variable, combined with penalizing their gradients, leads to continuous fiber angles that are more continuous for manufacturability compared to direct optimization results, although this approach requires roughly three times the optimization time.
- The objective function to maximize the critical load ratio is suitable only for load boundary conditions. The optimization formulation must be modified to account for the change in reaction forces when Dirichlet boundary conditions were used because the optimization formulation is valid only when the reaction forces remain constant under Neumann boundary conditions [22].
- The improvement in the critical buckling load ratio is consistent with their findings, but less than in the case of unidirectional lamina with 90° in the critical buckling load because the in-plane reaction forces under displacement boundary conditions also change during optimization and must be taken into account.
- The out-of-plane boundary conditions for compression buckling were of simply supported type in several studies [31,46,47]. However, from a practical testing point of view, maintaining this boundary condition during a compression experiment is practically challenging. Therefore, optimization is also performed for a plate with two opposite edges free and the other two edges as the clamped. Optimization using variable stiffness revealed straight fibers in approximately the 90° direction, which is consistent with the CS findings for the force inputs. The resulting critical load ratio is 38% less than that of the simply supported case.
- The application of least squares and the continuity constraint on the lamination parameters implicitly during the optimization rather than explicitly as in the Refs. [34,41,42,49], increases the number of iterations in the optimization, but ensures the optimum fiber angles.
- The optimal variable stiffness solution in [46] is implemented as a user-defined material model in Abaqus UMAT® to allow the testing of different designs for various applications, including quasi-static loading and buckling analyses.

Future research entails applying the developed design methodology to manufacturing using the AFP process and subsequently experimental testing of the produced variable stiffness. The presence of defects and artifacts during the AFP process must be investigated. Similarly, the buckling behavior under other boundary conditions for shear and biaxial loads shall be investigated.

CRediT authorship contribution statement

Eralp Demir: Writing – review & editing, Writing – original draft, Visualization, Software, Methodology, Investigation, Formal analysis, Data curation, Conceptualization. **Ali Rashed:** Writing – review & editing, Visualization.

Declaration of competing interest

The authors declare that they have no known competing financial interests or personal relationships that could have appeared to influence the work reported in this paper.

Appendix A. Mesh convergence

Plate buckling is performed using different mesh sizes of 5, 10, 15, and 20 elements per edge of a square plate, giving a total number of 25, 100, 225, and 400 elements. CCFF-SSSS boundary conditions with the uniform edge displacement and material properties in Table 1 are utilized. A laminate with a single constant fiber angle of 0° is used. The relative errors in the critical load ratio are 1.15%, 0.07% and 0.01% respectively for 5, 10, and 15 elements per edge with respect to 20 divisions per edge. Therefore, the mesh with 15 elements per edge has enough mesh refinement to represent the mode shapes, and hence it is used to perform optimization within the minimum possible computational times.

Appendix B. Gradient of the objective function by numerical perturbation

The gradient of the objective function is checked using a numerical perturbation. For this reason, the objective function is computed for every perturbed value of the lamination parameter $\widetilde{\xi}_j^i$:

$$(\widetilde{\xi}_j^i)_k = (\xi_j^i)_k + \varepsilon. \tag{B.1}$$

The magnitude of the perturbation step, ε, was 10^{-3}. ξ_j^i is the lamination parameter in which the superscript i represents the type of the parameter (A: in-plane, or, D: out-of-plane) while the subscript j stands for the component of the lamination parameter (1 or 3). The subscript k represents the number of elements. The simulations were performed for a plate with 25 elements to be able to do the perturbation in reasonable computational times. The displacement boundary conditions were used together with the fixed degrees of freedom according to the CCFF-SSSS case, which is shown in Fig. 3(a).

The numerical perturbation is applied to each of the lamination parameters of i and j; and for each element k to obtain the sensitivity of the objective function, $\widetilde{\lambda}_1$:

$$\frac{\partial \lambda_1}{\partial (\xi_j^i)_k} \approx \frac{\widetilde{\lambda}_1 - \lambda_1}{\varepsilon}. \tag{B.2}$$

The optimization performance and robustness are checked by using different types of gradient of the objective function (a) analytical gradient, (b) gradient obtained by numerical perturbation, (c) by setting the fmincon option "SpecifyObjectiveGradient" to "false", and (e) analytical gradient of the objective function together with the Hessian, that is, for the nonlinear constraints. Table B.1 shows the results obtained for computational times and the number of calls and iterations of functions are provided for a plate with five divisions CCFF/SSSS in-plane/out-of-plane boundary conditions and for the material properties shown in Table 1. The convergence tolerances ("ConstraintTolerance", "StepTolerance", and "OptimalityTolerance") were all set to 10^{-6}. Although the number of iterations looks nearly the same for all cases, the function calls become extremely high when no gradient is defined, Table B.1, case without (fmincon). In addition, when numerical perturbation is used, the computational time increases nearly four times more than that of the analytical. Therefore, the analytical expression for the calculation of the objective function gradient, no matter how complicated the definition is, is essential for the efficiency of gradient-based optimizers.

The number of iterations to converge for all cases is too high due to the small convergence tolerance selected. Fig. B.1 shows the convergence of the objective function. The convergence rate is significantly improved when the Hessian is provided in comparison to just using the analytical gradient for the objective function. However, the objective function becomes better than the optimum but compromising the feasibility. The number of function calls exceed the limit (50,000) used in the case when the default gradient is used (fmincon-default) due to the very slow convergence rate after 100–200 iterations, as can be seen from Fig. B.1. Fig. B.2 shows the distribution of the square norm for the lamination parameters, $\|\xi\|$, to provide a comparison of the robustness of the gradient calculation. The difference in the use of the analytical gradient in Fig. B.2(a) and the perturbation in Fig. B.2(b) is negligible. Fig. B.2(c) shows the optimization results when using the analytical gradient with the Hessian, revealing a negligible difference from other findings. The optimization results are different due to immature convergence when the gradient of the objective function is not specified as shown for the fmincon-default case in Fig. B.2(d). A coarse mesh was used because of the significant increase in computational

Table B.1
Comparison of different methods to calculate the gradient of the objective function: analytical, numerical perturbation, without the gradient of the objective function (fmincon default), and the analytical gradient together with the Hessian for the non-linear constraints.

	Analytical	Perturbation	Without (fmincon)	Analytical with the Hessian
Iterations	496	468	487	342
Function calls	801	952	50 013	1457
Time [s]	562.1	2192.5	1167.2	1000.6
Convergence	Yes	Yes	No (reached max.)	Yes

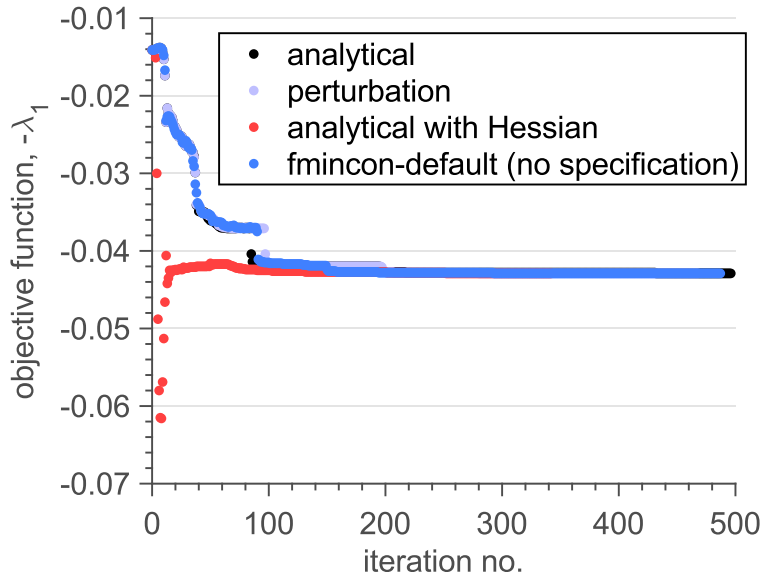


Fig. B.1. Number of iterations for different schemes to calculate the gradient of the objective function (a) analytical, (b) numerical perturbation, (c) analytical with Hessian, and (d) "fmincon" default (no specification of the objective function gradient). The division per edge of the plate was five and the boundary conditions were CCFF-SSSS.

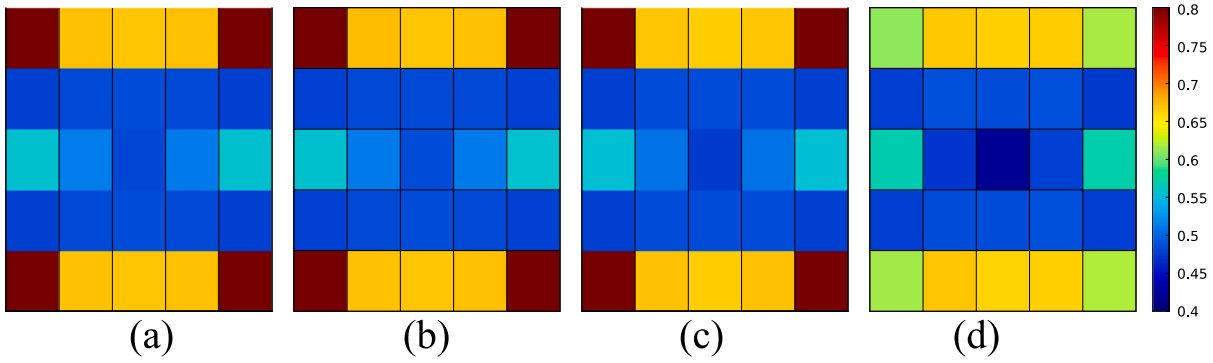


Fig. B.2. Norm of the lamination parameter distributions for different schemes to calculate the gradient of the objective function (a) analytical, (b) numerical perturbation, (c) analytical with Hessian, and (d) fmincon-default (no specification of the objective function gradient). The division per edge of the plate was five and the boundary conditions were CCFF-SSSS.

time that highlights the importance of analytical objective function gradient.

Appendix C. Hessian for the non-linear optimization constraints

The Hessian entails the second order derivative of the objective function and its constraints. The objective function is a function of bending and membrane stiffness terms that are both linear functions of the lamination parameters; hence, the Hessian of the objective function vanishes. However, the Hessian of the nonlinear constraints, g_i, are nonzero only:

$$H = \begin{bmatrix} \frac{\partial^2 g_i}{\partial \xi_1^A \partial \xi_1^A} & \frac{\partial^2 g_i}{\partial \xi_1^A \partial \xi_3^A} & \frac{\partial^2 g_i}{\partial \xi_1^A \partial \xi_1^D} & \frac{\partial^2 g_i}{\partial \xi_1^A \partial \xi_3^D} \\ \frac{\partial^2 g_i}{\partial \xi_3^A \partial \xi_1^A} & \frac{\partial^2 g_i}{\partial \xi_3^A \partial \xi_3^A} & \frac{\partial^2 g_i}{\partial \xi_3^A \partial \xi_1^D} & \frac{\partial^2 g_i}{\partial \xi_3^A \partial \xi_3^D} \\ \frac{\partial^2 g_i}{\partial \xi_1^D \partial \xi_1^A} & \frac{\partial^2 g_i}{\partial \xi_1^D \partial \xi_3^A} & \frac{\partial^2 g_i}{\partial \xi_1^D \partial \xi_1^D} & \frac{\partial^2 g_i}{\partial \xi_1^D \partial \xi_3^D} \\ \frac{\partial^2 g_i}{\partial \xi_3^D \partial \xi_1^A} & \frac{\partial^2 g_i}{\partial \xi_3^D \partial \xi_3^A} & \frac{\partial^2 g_i}{\partial \xi_3^D \partial \xi_1^D} & \frac{\partial^2 g_i}{\partial \xi_3^D \partial \xi_3^D} \end{bmatrix}. \quad \text{(C.1)}$$

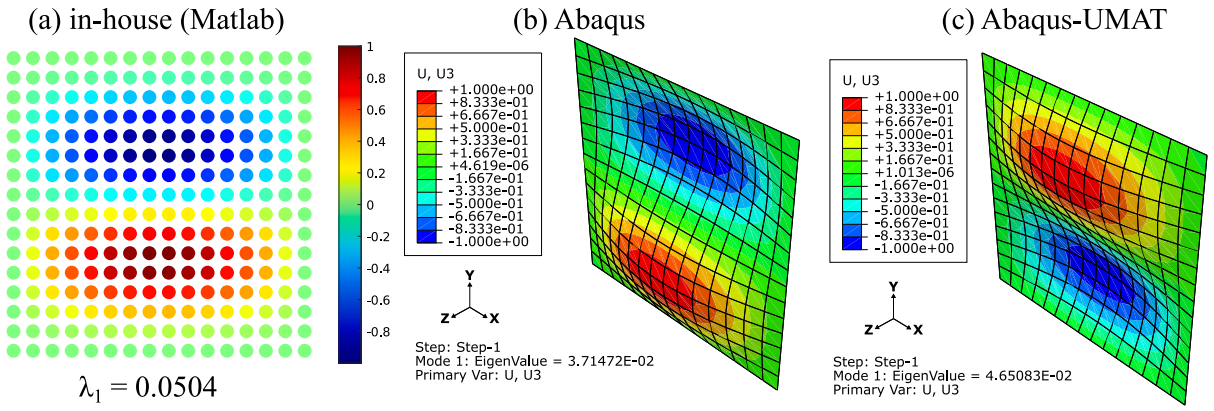


Fig. D.1. The first mode shape for $[90°]_8$ CS laminate obtained using (a) in-house Matlab® code, (b) default material model of Abaqus®, and (c) Abaqus®-UMAT. The plate has 15 elements per edge, material properties were the same as in Table 1, and the boundary conditions were CCFF-SSSS.

Therefore, the Hessian for Eq. (35) for the constraint g_1:

$$H_{g_1} = \begin{bmatrix} 18 & 0 & 10 & 0 \\ 0 & 0 & 0 & 0 \\ -10 & 0 & -10 & 0 \\ 0 & 0 & 0 & 0 \end{bmatrix}. \tag{C.2}$$

Similarly for Eq. (36) for the constraint functions of g_{2-10}:

$$H_{g_{2-10}} = \begin{bmatrix} 96t(\xi_3^A - 4t\xi_1^A + 1 + 2t^2) & -24t(\xi_3^A - 4t\xi_1^A + 1 + 2t^2) & 0 & 0 \\ -24t(\xi_3^A - 4t\xi_1^A + 1 + 2t^2) & 6(\xi_3^A - 4t\xi_1^A + 1 + 2t^2) & 0 & 0 \\ 0 & 0 & 0 & 0 \\ 0 & 0 & 0 & 0 \end{bmatrix}. \tag{C.3}$$

and for Eq. (37) that correspond to the constraint functions of g_{11-19}:

$$H_{g_{11-19}} = \begin{bmatrix} 96t^2(4t\xi_1^A - \xi_3^A + 1 + 4|t|) & -24t(4t\xi_1^A - \xi_3^A + 1 + 4|t|) & 0 & 0 \\ -24t(4t\xi_1^A - \xi_3^A + 1 + 4|t|) & 6(4t\xi_1^A - \xi_3^A + 1 + 4|t|) & 0 & 0 \\ 0 & 0 & 0 & 0 \\ 0 & 0 & 0 & 0 \end{bmatrix}. \tag{C.4}$$

These derivative terms have a consistent ordering as the design variables that are the four lamination parameters for each element for a variable stiffness case as shown in Eq. (34). The custom Hessian definition for fmincon using the "HessianFcn" option.

Appendix D. Abaqus® and UMAT

Unidirectional CS plates are used to compare the findings of the in-house Matlab® code with a commercial software. For this reason, Abaqus® is used as a commercial finite element software. Two different methods are used: (a) by using the buckling and quasi-static solutions for the principal eigenfrequency, λ_1, the reaction forces, $|R_y|$, and the critical buckling load, $|F_{cr}|$, using the default analysis available within the commercial software, and (b) by using the user-defined material model (Abaqus®-UMAT) for the buckling and static solutions. Simulations are performed for the boundary conditions in and out of the plane of CCFF-SSSS as shown in Fig. 3(a) by using the material parameters in Table 1.

Table D.1 shows the first buckling load ratio, reaction force along the loading direction, and buckling loads for two cases of UD. The reaction forces of the in-house code for the $[90]_8$ and $[0]_8$ composites agree well with both Abaqus® findings. However, the eigenfrequencies ($|\lambda_1|$) and therefore the critical buckling loads ($|F_{cr}|$) are very different. This is related to a different normalization used in Abaqus®

Table D.1
Comparison of the in-house finite element code with Abaqus®: critical load ratio (λ_1), total reaction force along the direction of loading (R_y), critical buckling load (F_{cr}), and corresponding layup sequence for uniform lamina layer thickness.

Laminate	Unidirectional (CS)	Unidirectional (CS)
Layup sequence	$[90°]_8$	$[0°]_8$
$\|\lambda_1\|$ (in-house Matlab®)	0.0141	0.0504
$\|\lambda_1\|$ (Abaqus®)	0.0041	0.0371
$\|\lambda_1\|$ (Abaqus®-UMAT)	0.0046	0.0465
$\|R_y\|$ (in-house Matlab®)	184.241	10.442
$\|R_y\|$ (Abaqus®)	184.243	10.442
$\|R_y\|$ (Abaqus®-UMAT)	187.620	10.609
$\|F_{cr}\|$ (in-house Matlab®)	2.598	0.527
$\|F_{cr}\|$ (Abaqus®)	0.755	0.387
$\|F_{cr}\|$ (Abaqus®-UMAT)	0.861	0.493

than the generalized eigenvalue function in Matlab®. Another source of this difference might be related to the use of shell-type elements in compression buckling simulations in Abaqus® that require non-zero transverse shear stiffness than that of the in-house code which uses BFS-type elements without the transverse shear loads. Abaqus® strictly demands nonzero values for transverse shear stiffness to obtain a solution; therefore, very large magnitudes (10^9 MPa) were used to obtain negligible transverse shear displacements and eliminate the appearance of the corresponding modes. The default Abaqus® model uses a through-thickness integration method, and so the UMAT entry occurs as many times through the thickness during the solution, pointing out the use of a different numerical solution procedure when using the default material model than the in-house code. For all these differences, the buckling frequencies are significantly different in the in-house code than the commercial software. However, the difference is less than 10% in most cases within the solvers of the commercial software.

Fig. D.1 shows the out-of-plane displacement corresponding to the first mode for $[0]_8$ layup obtained by the in-house Matlab® code, the default Abaqus® analysis and the UMAT subroutine of Abaqus®. Note that the buckling modes are quite consistent and match well with the in-house code but different magnitudes of the eigenvalues. Even Abaqus® reveals different eigenvalues when the default analysis and the UMAT results are compared. The buckling mode when loading $[0]_8$ setup becomes higher order when loaded along the transverse direction with respect to the fiber axis, which is observed by all methods. Although the magnitudes of the eigenfrequencies are different between the in-house code and the commercial software, the mode shapes being approximately the same validates the buckling approach of the in-house Matlab® code.

Table E.1
Description of function files for finite element calculations ("FEM_") and optimization ("OPT_").

Prefix	"FEM_"	"OPT_"
Suffix	"inputs": FE model inputs "applybcs": application of BCs "assemble": FE assembly "bmat": bending strain - displacement "elementdof": to calculate element dof "elmass": element mass matrix "elstiff": element stiffness matrix "fedlw": distributed edge load along z-dir. "fedlu": distributed edge load along x-dir. "fedlv": distributed edge load along y-dir. "fpl": body force "fsdlw": distributed pressure load "geostiffness": geometric stiffness calculation "intialize": initialization "lam": buckling calculations "modifystiffness": stiffness modifications "nmat": shape function calculator "output": output calculations "output_ms": mode shape calculations	"inputs": Optimization related inputs "constraint_con": constraints for CS case "constraint_var": constraints for VS case "constraint_fun": contraint function "objective_con": objective function for CS case "objective_var": objective function for VS case "output_nod": output nodal variables "output_el": output elemental variables "output_lp": output lamination parameters "tangent": sensitivity of lamination parameters

Table E.2
Description of function files for least-squares and continuity constraints ("LSC_"), lamination parameters ("LP_") and material properties ("MAT_").

Prefix	"LSC_"	Prefix	"LP_"
Suffix	"inputs": Least-Squares and Continuity constraints "LP": calculates lamination parameters "LP0": calculation lamination parameters at the element centers "AssembleFvec": assembles the force-like vector of lamination parameters "assemblecons": assembles the mass-like matrix for lamination parameters "cmat": calculate $[\boldsymbol{C}]$ matrix "mmat": calcualte $[\boldsymbol{M}]$ matrix "initialize": initialize calculations once "lpdist": apply constraints and solve for nodal values of lamination parameters "n": calculate shape functions "n0": calculate shape functions at the element centers "nder": calculate shape function derivatives "sfder": calculate spatial gradients	Suffix	"inputs": Lamination parameter library "find": find the layup sequence closest to the optimum "perm": permutation to obtain possible layup sequences "space": construct the lamination parameter space or library
		Prefix	"MAT_"
		Suffix	"inputs": material "Qbar": calculate reduced stiffness matrix "lp": calculate lamination parameters for a laminate "stiffness": calculate stiffness for a laminate "stiffnesslp": calculate stiffness for lamination parameters

Appendix E. In-house code structure

The code is prepared in Matlab® consisting of various functions in m-file format. The runner file is "MAIN.m". The m-files with the prefixes "FEM", "MAT", "LP", "LSC", and "OPT" contain the functions related to the finite element analysis for buckling, material stiffness, lamination parameters, discretized least-squares constraints on lamination parameters, and optimization, respectively. Tables in E.1 and E.2 show a brief description of each function.

Data availability

The source code utilized for the data generation is accessible as open source at the provided Github link: https://github.com/EralpDemir/Composite-Materials.

References

[1] Oromiehie E, Prusty BG, Compston P, Rajan G. Automated fibre placement based composite structures: Review on the defects, impacts and inspections techniques. Compos Struct 2019;224:110987.

[2] Bakhshi N, Hojjati M. An experimental and simulative study on the defects appeared during tow steering in automated fiber placement. Compos Part A: Appl Sci Manuf 2018;113:122–31.

[3] Abera T, Beom-Soo K. Elastic deformation of fiber-reinforced multi-layered composite cylindrical shells of variable stiffness. Compos Part B: Eng 2016;100:44–55.

[4] Mohammad R, Hossein G, Suong V, Mehdi H. Multi-objective design optimization of variable stiffness composite cylinders. Compos Part B: Eng 2015;69:249–55.

[5] Falcóa O, Mayugoa J, Lopes C, Gascons N, Turona A, Costa J. Variable-stiffness composite panels: As-manufactured modeling and its influence on the failure behavior. Compos Part B: Eng 2014;56:660–9.

[6] Viglietti A, Zappino E, Carrera E. Analysis of variable angle tow composites structures using variable kinematic models. Compos Part B: Eng 2019;171:272–83.

[7] Air A, Prusty BG. Manufacturing feasibility of a bend free ellipsoidal composite pressure vessel using automated fibre placement. Compos Part A: Appl Sci Manuf 2023;107968.

[8] Awad ZK, Aravinthan T, Zhuge Y, Gonzalez F. A review of optimization techniques used in the design of fibre composite structures for civil engineering applications. Mater Des 2012;33:534–44.

[9] Albazzan MA, Harik R, Tatting BF, Gürdal Z. Efficient design optimization of nonconventional laminated composites using lamination parameters: A state of the art. Compos Struct 2019;209:362–74.

[10] Sørensen R, Lund E. Thickness filters for gradient based multi-material and thickness optimization of laminated composite structures. Struct Multidiscip Optim 2015;52(2):227–50.

[11] Vo-Duy T, Ho-Huu V, Do-Thi T, Dang-Trung H, Nguyen-Thoi T. A global numerical approach for lightweight design optimization of laminated composite plates subjected to frequency constraints. Compos Struct 2017;159:646–55.
[12] Groenwold AA, Haftka RT. Optimization with non-homogeneous failure criteria like Tsai–Wu for composite laminates. Struct Multidiscip Optim 2006;32(3):183–90.
[13] Lopez R, Luersen M, Cursi E. Optimization of laminated composites considering different failure criteria. Compos Part B: Eng 2009;40(8):731–40.
[14] Khani A, IJsselmuiden ST, Abdalla MM, Gürdal Z. Design of variable stiffness panels for maximum strength using lamination parameters. Compos Part B: Eng 2011;42(3):546–52.
[15] Le-Manh T, Lee J. Stacking sequence optimization for maximum strengths of laminated composite plates using genetic algorithm and isogeometric analysis. Compos Struct 2014;116:357–63.
[16] Stegmann J, Lund E. Discrete material optimization of general composite shell structures. Internat J Numer Methods Engrg 2005;62(14):2009–27.
[17] Setoodeh S, Abdalla MM, Gürdal Z. Design of variable–stiffness laminates using lamination parameters. Compos Part B: Eng 2006;37(4–5):301–9.
[18] Dutra TA, de Almeida SFM. Composite plate stiffness multicriteria optimization using lamination parameters. Compos Struct 2015;133:166–77.
[19] Diaconu C, Sato M, Sekine H. Layup optimization of symmetrically laminated thick plates for fundamental frequencies using lamination parameters. Struct Multidiscip Optim 2002;24(4):302–11.
[20] Narita Y, Hodgkinson J. Layerwise optimisation for maximising the fundamental frequencies of point-supported rectangular laminated composite plates. Compos Struct 2005;69(2):127–35.
[21] Apalak ZG, Apalak MK, Ekici R, Yildirim M. Layer optimization for maximum fundamental frequency of rigid point-supported laminated composite plates. Polym Compos 2011;32(12):1988–2000.
[22] Foldager J, Hansen J, Olhoff N. Optimization of the buckling load for composite structures taking thermal effects into account. Struct Multidiscip Optim 2001;21(1):14–31.
[23] Bloomfield MW, Herencia JE, Weaver PM. Enhanced two-level optimization of anisotropic laminated composite plates with strength and buckling constraints. Thin-Walled Struct 2009;47(11):1161–7.
[24] Topal U, Uzman Ü. Effects of nonuniform boundary conditions on the buckling load optimization of laminated composite plates. Mater Des 2009;30(3):710–7.
[25] Lindgaard E, Lund E. Optimization formulations for the maximum nonlinear buckling load of composite structures. Struct Multidiscip Optim 2011;43(5):631–46.
[26] Ehsani A, Rezaeepazhand J. Stacking sequence optimization of laminated composite grid plates for maximum buckling load using genetic algorithm. Int J Mech Sci 2016;119:97–106.
[27] Ho-Huu V, Do-Thi T, Dang-Trung H, Vo-Duy T, Nguyen-Thoi T. Optimization of laminated composite plates for maximizing buckling load using improved differential evolution and smoothed finite element method. Compos Struct 2016;146:132–47.
[28] Henrichsen SR, Weaver PM, Lindgaard E, Lund E. Post-buckling optimization of composite structures using koiter's method. Internat J Numer Methods Engrg 2016;108(8):902–40.
[29] Fukunaga H, Sekine H. Stiffness design method of symmetric laminates using lamination parameters. AIAA J 1992;30(11):2791–3.
[30] Diaconu CG, Sato M, Sekine H. Feasible region in general design space of lamination parameters for laminated composites. AIAA J 2002;40(3):559–65.
[31] Wu Z, Raju G, Weaver PM. Framework for the buckling optimization of variable-angle tow composite plates. AIAA J 2015;53(12):3788–804.
[32] Grenestedt J, Gudmundson P. Layup optimization of composite material structures. Optim Des Adv Mater 1993;311–36.
[33] IJsselmuiden ST, Abdalla MM, Seresta O, Gürdal Z. Multi-step blended stacking sequence design of panel assemblies with buckling constraints. Compos Part B: Eng 2009;40(4):329–36.
[34] Demir E, Yousefi-Louyeh P, Yildiz M. Design of variable stiffness composite structures using lamination parameters with fiber steering constraint. Compos Part B: Eng 2019;165:733–46.
[35] Hong Z, Peeters D, Turteltaub S. An enhanced curvature-constrained design method for manufacturable variable stiffness composite laminates. Comput Struct 2020;238:106284.
[36] Van Campen JM, Kassapoglou C, Gürdal Z. Generating realistic laminate fiber angle distributions for optimal variable stiffness laminates. Compos Part B: Eng 2012;43(2):354–60.
[37] Peeters DM, Lozano GG, Abdalla MM. Effect of steering limit constraints on the performance of variable stiffness laminates. Comput Struct 2018;196:94–111.
[38] Panettieri E, Montemurro M, Catapano A. Blending constraints for composite laminates in polar parameters space. Compos Part B: Eng 2019;168:448–57.
[39] Setoodeh S, Gürdal Z, Watson LT. Design of variable-stiffness composite layers using cellular automata. Comput Methods Appl Mech Engrg 2006;195(9–12):836–51.
[40] Hao P, Yuan X, Liu H, Wang B, Liu C, Yang D, Zhan S. Isogeometric buckling analysis of composite variable-stiffness panels. Compos Struct 2017;165:192–208.
[41] Shafighfard T, Demir E, Yildiz M. Design of fiber-reinforced variable-stiffness composites for different open-hole geometries with fiber continuity and curvature constraints. Compos Struct 2019;226:111280.
[42] Shafighfard T, Cender TA, Demir E. Additive manufacturing of compliance optimized variable stiffness composites through short fiber alignment along curvilinear paths. Addit Manuf 2021;37:101728.
[43] Hao P, Liu C, Yuan X, Wang B, Li G, Zhu T, Niu F. Buckling optimization of variable-stiffness composite panels based on flow field function. Compos Struct 2017;181:240–55.
[44] Vasileios S, Chitrang P, Ali Y. Stiffness-based optimization framework for the topology and fiber paths of continuous fiber composites. Compos Part B: Eng 2020;183(107681).
[45] Tian Y, Pu S, Zong Z, Shi T, Xia Q. Optimization of variable stiffness laminates with gap-overlap and curvature constraints. Compos Struct 2019;230:111494.
[46] Gürdal Z, Tatting BF, Wu C. Variable stiffness composite panels: effects of stiffness variation on the in-plane and buckling response. Compos Part A: Appl Sci Manuf 2008;39(5):911–22.
[47] Hao P, Liu D, Wang Y, Liu X, Wang B, Li G, Feng S. Design of manufacturable fiber path for variable-stiffness panels based on lamination parameters. Compos Struct 2019;219:158–69.
[48] Foldager J, Hansen J, Olhoff N. A general approach forcing convexity of ply angle optimization in composite laminates. Struct Optim 1998;16:201–11.
[49] Rashed A, Demir E. Design of variable stiffness composites for maximum fundamental frequency considering manufacturing constraints of tow steering. Compos Struct 2022;284:115151.
[50] Caprino G, Visconti IC. A note on specially orthotropic laminates. J Compos Mater 1982;16(5):395–9.
[51] Blom AW, Abdalla MM, Gürdal Z. Optimization of course locations in fiber-placed panels for general fiber angle distributions. Compos Sci Technol 2010;70(4):564–70.
[52] Demir E. Github page, https://github.com/EralpDemir/Composite-Materials, [Accessed 11 August 2024].
[53] Wu Z, Weaver PM, Raju G, Kim BC. Buckling analysis and optimisation of variable angle tow composite plates. Thin-Walled Struct 2012;60:163–72.
[54] Setoodeh S, Abdalla MM, IJsselmuiden ST, Gürdal Z. Design of variable-stiffness composite panels for maximum buckling load. Compos Struct 2009;87(1):109–17.
[55] IJsselmuiden ST, Abdalla MM, Gurdal Z. Optimization of variable-stiffness panels for maximum buckling load using lamination parameters. AIAA J 2010;48(1):134–43.
[56] IJsselmuiden ST, Abdalla MM, Gurdal Z. Optimization of variable-stiffness panels for maximum buckling load using lamination parameters. AIAA J 2010;48:134–43.
[57] Marouene A, Boukhili R, Chen J, Yousefpour A. Effects of gaps and overlaps on the buckling behavior of an optimally designed variable-stiffness composite laminates – a numerical and experimental study. Compos Struct 2016;140:556–66.
[58] Marouene A, Boukhili R, Chen J, Yousefpour A. Buckling behavior of variable-stiffness composite laminates manufactured by the tow-drop method. Compos Struct 2016;139:243–53.
[59] Hibbitt, Karlsson, Sorensen. ABAQUS/Standard: User's Manual. Vol. 1, Hibbitt, Karlsson & Sorensen; 1997.